Design, Fabrication and Analysis of a Piezoelectric Nanocomposite Paint

By

Samuel A. Osho

A thesis submitted to the Faculty of Graduate Studies of The University of Manitoba in partial fulfillment of the requirements of the degree of

MASTER OF SCIENCE

Department of Mechanical Engineering
University of Manitoba
Winnipeg, Manitoba

Abstract

The recent progress in technology has resulted in the maintenance of structures being carried out through Structural Health Monitoring (SHM). The primary aim of SHM is early detection and location of damage in structures. Despite the different techniques available in SHM, engineers opt for piezoelectric sensors in a bid to achieve their goals. In this research, a theoretical model that shows the feasibility of using a damage detection sensor capable of multipoint strain sensing is developed. The multi-point strain sensing coating applied to the top-surface layer of a delaminated cantilever beam detected the presence and location of delamination in the beam. The theoretical model serves as the basis to produce a piezoelectric nanocomposite paint with possible applications as dynamic strain sensors and/or piezoelectric transducers. The coating is in form of a low-cost paint, which is flexible and bonds strongly on a metallic surface via the solvent-casting method. The nanocomposite is produced by an ultrasonic mixture of varying percentages of Zinc oxide nanopowder water dispersion, Poly Vinyl Acetate glue (PVA) and Carbon nanotubes (CNTs). Transmission Electron Microscopy (TEM) images confirmed the linkages of zinc oxide (ZnO) nanoparticles in the composite by CNTs. The optimum mixing ratio with the highest piezoelectricity is 78.1% ZnO, 19.5% PVA glue and 2.4% multi-wall carbon nanotubes (MWCNTs). Results of the characterization of the nanocomposite paint indicate that the mechanical and piezoelectric properties of the nano-composite paint reached a threshold point in the increment of CNTs to the paint before showing signs of decline.

Acknowledgments

My sincere appreciation goes to my amazing supervisors: Dr. Nan Wu and Dr. Olanrewaju Ojo. I am grateful for their consistent guidance, steady support, energizing words of encouragement and priceless ideas during my Master's program and most especially while preparing my thesis. They made themselves available when I needed help during my research and offered invaluable advice. I would also like to appreciate Dr. Malcolm Xing for granting me the permission to use the ultrasonic machine in his laboratory which was an important part of my research work.

I would also like to thank my colleagues in our research group; those intellectual discussions broadened my horizon. My appreciation also goes to a league of my exceptional friends who offered support and motivation while I was writing the thesis: Victoria Ibiwoye, Mayowa Tijani, Taiwo Dada, Philip Olabisi, and Abisola Otesile.

This would have been impossible without the unconditional love and constant support of my family; thanks to my wonderful parents and lovely siblings.

Finally, thanks to the Almighty God for the strength, wisdom, and ability to complete my Master program and to write this thesis. I am grateful!

Table of Contents

List of Figures

List of Tables

List of Symbols

a : Length of the delaminated section

A_1 : Surface area of the electrode

A_2 : Surface area of the tip of the force transducer

b : the width of the cantilever steel beam

C_v : Electrical capacity of the PZT coating

C : Capacitance

D : Charging density

d_{33} : Piezoelectric coupling coefficient for Strain-Charge form

E : The Young's Modulus

F : Force

H : Thickness of the cantilever beam

h_1 : Thickness of the PZT coating on the beam.

I : Moment of Inertia

L : Length of the cantilever beam

L_1 : Distance between the fixed end of the beam and the beginning of delamination

L_2 : Distance between the fixed end of the beam and the end of delamination

M : Bending Moment of the cantilever beam

ρ : Mass-density of the cantilever beam

Q : Electrical charge

S : Stress

V : Voltage

ω : Natural frequency of the beam

w : Deflection of the cantilever beam

$W(x)$: Sum of nth mode shapes

Chapter 1 Introduction

1.1 Background

In recent times, there has been a significant increase in technologies used for effective monitoring and maintenance of structures. During the usage of a structure, its members undergo gradual deterioration which is usually because of the dynamic loadings, static loadings and a host of other environmental factors. Damage can happen as alterations introduced into a system and produce unwanted effects in the present and future performances of the system. These changes in the system include material property changes, changes in boundary conditions, and changes in system connectivity [1], which can cause the failure of the whole engineering systems and even disasters if left without attention.

Structural health monitoring (SHM) caters for the health of structures; it is a form of technology that makes use of a set of proven techniques and methods for early detection and location of damage in structures. Different structure types are susceptible to distinct forms of damage but SHM comes up with innovative ways to detect damage, manage the health status of these structures and hence avoid sudden failures. It is certain that damage will occur in structures due to the excitation they undergo during usage but the monitoring techniques ascertain that the impact damage is detected early.

Furthermore, there are several damage detection methods which include frequency changes [2][3], mode shape changes, dynamically measured flexibility, optical fiber methods [4][5], ultrasonic waves methods [6], neural network-based methods [7], acoustic emission methods, matrix update methods, piezoelectric transducers [8], non-linear methods and many more.

In the class of non-destructive techniques for damage detection, Rahman et al. [2] investigated the effects of open cracks in rotor shaft using changes in frequency response function (FRF) phase. The acceleration frequency responses at different points on rotor shafts were measured, it was concluded that the vibration behavior of the rotor shaft is extremely sensitive to crack depth, crack location and mode number. Duggan and Ochoa [3] characterized the effect of material system, geometry and stacking sequence on the vibration responses of damaged fiber reinforced composite plates. The study focused on the alteration of the natural frequencies of damaged composite materials and its implications on damage detection in structures. Al-Said and Al-Qaisia [9] investigated the effect of locations of attached masses and crack depth on the alteration of the natural frequency of a system. This was done via the free vibration of a clamped-clamped cracked beam with different attached point loads along the length of the beam.

However, in the modern-day SHM solutions, engineers make attempts to produce sensors that can work perfectly for structures that need flexibility due to their geometrical constraints. The focus of this research work is to expand the frontiers of possible applications of a flexible piezoelectric sensor in SHM.

Lots of the sensors with SHM applications are made of smart materials with a strong predilection for piezoelectric materials. There are several materials that exhibit piezoelectricity and they include Lead Zirconate Titanate (PZT), Poly Vinylidene Fluoride (PVDF), barium titanate ($BaTiO_3$) and zinc oxide (ZnO). Each of these materials has its own limitations and strengths in SHM applications. The most widely used piezoelectric material is PZT ceramics – it has the highest piezoelectric potential but its brittleness limits its usage on structures where flexibility is needed.

1.2 Motivation

In search of a better alternative to replace the brittleness of PZT ceramics, most researchers opt for other natural occurring piezoelectric materials, such as zinc oxide (ZnO), barium titanate ($BaTiO_3$), and poly vinylidene fluoride (PVDF), using them either singly or combining them with other flexible materials that can enhance their piezoelectric and mechanical performance. In the research conducted by Meyers et al.[10], ZnO nanoparticles were used for the enhancement of the piezoelectricity of a flexible piezoelectric polymer, Poly (vinylidene fluoride-trifluoroethylene) (PVDF-TrFe) via interdigitated transducers. Another study [11] reported the fabrication of a piezoelectric thin film made via the dispersion of zinc oxide nanoparticles in polymers - poly (sodium 4-styrenesulfonate) (PSS) and poly (vinyl alcohol) (PVA) using high-energy probe sonication.

There are a plethora of published work [10], [12]–[17] that have reported the fabrication of flexible piezoelectric nano-composite sensors. Most of the composites incorporate a flexible matrix that avoids the breakage and rupture of the embedded piezoelectric material when mechanically deformed. Gullapalli et al. [12] fabricated a flexible strain sensor by embedding crystalline piezoelectric material in a matrix made of cellulose fibers (paper). The nanocomposite strain sensor yielded excellent strain sensitivity when tested under static and dynamic loadings.

In addition, for the fabrication of nanocomposites, the most widely used techniques include: solvent casting [18][19], melt mixing [20], spin coating [14][21], in-situ polymerization [22][23], twin screw pulverization [24], latex fabrication[25][26], coagulation spinning [27], electrophoretic deposition[28], compression molding [29] and injection molding [20]. All these methods have their merits and demerits but the goal is to achieve homogeneity in the constituents of the composites which is dependent on a host of factors.

However, despite the outstanding contributions of these flexible composite sensors, they have demerits – complex and expensive fabrication procedures, low piezoelectric output, low mechanical strength and limited application for sensing because they are usually thin films attached on smooth surfaces of structures. With the advent of nanotechnology and its remarkable success stories, researchers have resorted to the use of nanomaterials like carbon nanotubes for enhancing the piezoelectric and mechanical performance of naturally-occurring piezoelectric materials, hence leading to the creation of piezoelectric nano-composites. Ramaratnam and Jalili [30] developed thin carbon nanotube-based piezoelectric PVDF-TrFe films to investigate the influence of Multi-Walled Carbon Nanotubes (MWCNT) and Single-Walled Carbon Nanotubes (SWCNT) on the sensitivity of piezoelectric polymers. For strain sensing applications, other studies [31][32] also reflect the possibility of using carbon nanotubes as one of the key materials in making the nanocomposite sensors [33].

Due to the great attention paid to developing technologies along the path of Structural Health Monitoring, numerous researchers have proposed the fabrication of several piezoelectric nanocomposites that possess excellent functionalities as sensors. However, one of the current limitations of these sensors is that they are merely films attached to discrete locations on the structure and cannot be applied to a large surface area on the host structure especially ones with a rough surface condition. There is a need to fabricate sensors capable of multipoint strain sensing; cover a large surface area and exhibit excellent flexibility.

1.3 Research Objectives

This research aims to develop a theoretical model that shows the feasibility of using a damage detection sensor capable of multipoint strain sensing. The theoretical model informs the second objective of producing a flexible and strong piezoelectric nanocomposite paint that has the capacity to provide multipoint strain sensing, bonds to metallic surfaces and can be used potentially as strain sensors in the field of Structural Health Monitoring.

1.4 Research Scope

The scope of this research work is limited to the use of zinc oxide nanoparticles and how its effectiveness can be optimized through the addition of CNTs. Zinc oxide is chosen because it exhibits the strongest piezoelectric coefficient in the category of other piezoelectric materials asides PZT ceramics[34], [35]. Only metallic surfaces (Stainless Steel) are considered during the application of the nanocomposite paint. The painted metallic beams are excited via static loadings during the piezoelectric calibration.

1.5 Methodology

To achieve the design, production, and analysis of the piezoelectric nanocomposite paint, the numerical modeling of a delaminated cantilever beam covered with a piezoelectric coating on its top surface is proposed. The numerical modeling and simulation are done via MATLAB with explicit calculations based on Euler-Bernoulli's theory of beams. The delamination introduced in the midsection of the beam altered its boundary condition; the changes in boundary condition paved way for the generation of the equations used for calculating the deflection, mode shapes and curvature distribution of the beam when subjected to harmonic loading.

The production of the piezoelectric nanocomposite paint is carried out through the ultrasonic mixing of zinc oxide nanoparticles dispersed in water, carbon nanotubes dispersed in water and polyvinyl acetate (PVA) glue, the resulting nanocomposite solution is applied on metallic surfaces via the solvent casting method. The stainless steel is used as the substrate and eight layers of the paint are applied on its surface to produce a coating of appreciable thickness in the range of 130-

150 µm. However, five different samples of the nanocomposite solution are prepared with respect to the increment in the weight percentages of carbon nanotubes.

Subsequently, the experimental procedures included the characterization of the mechanical and piezoelectric properties of the nanocomposite paint coupled with its microstructural study. The evaluation of the mechanical properties (Young's modulus and hardness) of the different paint samples is done via nano-indentation using the Oliver-Pharr method. The determination of its piezoelectric coefficients is conducted via the LMS Data Acquisition system which gives an accurate measurement of the static force applied and the voltage generated by the coating when mechanically deformed. The microstructural analysis of the nanocomposite paint is carried out using both the Transmission Emission Microscope (TEM) and the Nano-Scanning Electron Microscope (Nano-SEM).

1.6 Major Findings

The results of theoretical modeling of the delaminated cantilever beam when under harmonic excitation validate the feasibility of having a damage detection coating capable of multipoint sensing. These results informed the production of the piezoelectric nano-composite paint which is expected to act as a substitute for the piezoelectric coating used in the modeling.

Subsequently, the research work validates the possibility of producing a low-cost piezoelectric nanocomposite paint from the ultrasonic mixing of zinc oxide nanoparticles dispersion, Poly Vinyl Acetate (PVA) glue and carbon nanotubes, and applied on metallic surfaces via the solvent-casting method. It further reinforces the standing notion that the piezoelectric performance of composites made of zinc oxide nanoparticles can be enhanced by the addition of carbon nanotubes.

The piezoelectric calibration of the paint shows that there is a threshold amount of CNTs that can be added to the paint for an optimum piezoelectric performance. The nanoindentation of the coating formed from the paint reveals that there is a switch in the mechanical properties (Young's Modulus and Hardness) of the material at a certain proportion. The threshold amount of CNTs that can be added to the nanocomposite paint for optimized performance stands at 2.4%.

Furthermore, the microstructural investigation confirms the joining of zinc oxide nanoparticles by strings of carbon nanotubes and hence increase the number of possible conduction paths. The microstructure of the paint also gives information about the presence of voids in the paint when excess CNTs are added, thereby causing the decrease in its mechanical and piezoelectric properties.

1.7 Thesis Structure

The organization of thesis is as follows: Chapter 1 gives an overview of the introduction which consists of the background information, the motivation for the work, research objectives, research scope, methodology and the thesis structure. Chapter 2 provides a robust literature review on the principles of Structural Health Monitoring coupled with the growth of damage in structures, applications using piezoelectric composite materials with a focus on the use of zinc oxides and carbon nanotube-enhanced films. The different methods used in the fabrication of nanocomposites are also discussed.

Chapter 3 introduces the theoretical modeling and simulation of a delaminated beam with its top surface covered with a piezoelectric paint which depicts the possibility of producing a piezoelectric paint sensor capable of multipoint strain sensing. The simulation sheds clarity on the feasibility of the future applications of the nanocomposite paint fabricated as a major component of a damage detection technique. In chapter 4, five samples of piezoelectric nanocomposite paints are then produced using a low-cost method of solvent casting, and their mechanical properties and piezoelectric coefficient are experimentally tested to evaluate its feasibility as a surface paint. The main components of the nano-composite paint are zinc oxide nanoparticles dispersion, Carbon nanotubes (CNTs) and Polyvinyl acetate glue (PVA). The thesis ends with the statement and discussion of results in Chapter 5 alongside the major conclusions and future work in Chapter 6.

Chapter 2 Literature Review

In this section, an elaborate literature review of previous research work done by others regarding the use of piezoelectric materials in SHM is presented. The discussion entails a close review of recent work published in the applications of piezoelectric materials in damage detection as well as the current fabrication and calibration methods of different nano-composites.

2.1 Structural Health Monitoring Techniques

In the monitoring of health status of structures, it is challenging to know the type of alterations to look out for and the methods of identifying them [36]. The peculiarity of damage alterations that usually occurs in a structure will determine the type of sensor that can be employed in its damage detection.

2.1.1 Damage

During the lifecycle of a structure, it continually undergoes dynamic and static loadings which lead to wear and tear until they finally fail. This is usually in form of vibrations and oscillations due to the impact of an external loading. When a structure or a material experiences a breach in its optimum performance and deviates from its original characteristics, it is known as damage. However, damage develops gradually in structures and causes fatigue before the final failure or collapse.

Damage is commonly observed as cracks, notches, delamination, creep, and buckling. Damage in structures can either be inflicted internally or externally; the barely visible impact damage in the internal layer of a structure is very dangerous. Damage generally initiate alterations in the dynamic characteristics of the structures. These alterations include changes in natural frequencies, changes in mode-shapes and changes in damping ratios.

For mechanical and civil engineers, it is a compulsory task to consciously monitor the growth of damage in a structure over the period of its usage in a bid to avoid sudden failure which could be fatal or even has huge economic implications.

2.1.2 Causes of Damage

When structures are used, degradation sets in gradually over the course of the lifespan of the structure in form of varying degrees of impact damage. The degree of damage in a structure depends on the properties of the structure and the frequency of the impact load. For structures that are brittle, a sudden impact can lead to fracture due to the fast propagation of cracks in a short time. Malleable and ductile structures can withstand impact loads due to their elasticity. However, some structures could have enhanced mechanical properties during the process of production necessitated by the peculiarity of their usage. When a structure is used over time, the longer it is used, the more susceptible to damage it becomes. Fatigue also sets in due to cycling loading, Ruotsalainen et al. [37] did a study to effectively minimize fatigue damage in aircraft structures.

Some mechanical structures are used in harsh environments, especially environments that stimulate microbial activity for the initiation of corrosion. Corrosion is one of the major causes of damage in structures. It is purely the oxidation of metals – taking them back to their oxide states in the presence of oxygen and water. Corrosion causes the production of notches which eventually leads to initiation of cracks. Engineers, however, employ several methods in a bid to prevent or manage corrosion. It could be by producing an alloy with one of its constituents having a corrosion resistance ability like a Stainless Steel that contains varying amounts of Nickel (Ni), Iron (Fe) and Carbon(C). Other methods include painting, electroplating, and galvanizing.

Structures with mechanical and physical defects are susceptible to damages. These defects may be acquired during the process of production or during its early stage of use. The location of defects in structures is usually the point of initiation of damages that eventually lead to fracture or failure. Asides the points of defects, weld joints are stress raisers and usually serve as locations for damage initiation in structures. Vijayanand et al. [38] carried out a robust investigation to evaluate the damage initiation caused by the creep cavitation behavior in austenitic stainless steel fusion zone via thorough microstructural and finite element analysis.

Engineers draw information from the changes in the structures caused by the presence of damage; the information is used for proper evaluation of its state of health. The analysis of information given by these changes can be used to identify the existence, location, and magnitude of any type of damage in a structure.

Structural Health Monitoring (SHM) is an emerging discipline in engineering that secures the health of structures and ensures that they are safe for use during their lifespan. There are peculiar damages to different structures but SHM comes up with innovative ways to manage the health of these structures and hence avoid sudden failures.

2.1.3 Structural Health Monitoring

Monitoring the health status of a structure is synonymous to the job of a medical doctor that observes the medical condition of a patient. Structural Health Monitoring (SHM) is a technology that makes use of a set of proven techniques and methods for early detection and location of damages in structures. It is certain that damages will occur in structures due to the excitation they undergo during usage but the monitoring techniques ascertain that the impact damage is detected early. Hence, the need for structural health monitoring.

Structural Health Monitoring (SHM) signifies a system with the capacity to detect, recognize and interpret adverse alterations in a structure in order to improve reliability and reduce life-cycle costs[36]. The merits of using SHM system over the traditional inspection methods include reduced downtime, eradication of component tear-down and the potential prevention of failure during operations. The primary goal of SHM system is to act as a perfect substitute for current inspection cycles with an active and highly sensitive monitoring system[36]. This will increase the likelihood of detecting damage before total failure.

Due to repeated loading and unloading, the damage will eventually occur in a structure after prolonged usage. When the failure of a structure happens, the loss can be colossal and life-threatening – in cases of the collapse of a bridge or a high-rise building. These losses are avoidable if structural health monitoring is taken seriously and implemented in observing the behavior of these structures during usage. This is the essence of maintenance schemes with proven SHM techniques that can predict the location of a potential failure of a structure.

For the strategic application of SHM, Doebling and Farrar [1] highlighted Rytter's proposed system of classification for damage identification methods described in four levels:

- Level 1: Determination that damage is present in the structure.
- Level 2: Determination of the geometric location of the damage.
- Level 3: Quantification of the severity of the damage
- Level 4: Prediction of the remaining service life of the structure

In the field of SHM, there are several methods used by engineers in achieving the goals of the four levels of damage identification as proposed by Rytter. These methods include frequency changes [2][3], mode shape changes, dynamically measured flexibility, optical fiber methods [4][5], ultrasonic waves methods [6], neural network-based methods [7], acoustic emission methods, matrix update methods, piezoelectric transducers [8], nonlinear methods and many more. The use of piezoelectric sensors and actuators is very pivotal to the success of these SHM techniques.

There are different SHM techniques used for investigation and evaluation of the severity of damage in structures. Barazanchy et al. [4] investigated the potential of using a hybrid structural health monitoring (SHM) system for detection and localization of damage in aerospace structures. The proposed hybrid system, a combination of a piezoelectric transducer and fiber-optic sensors (FOS) for generating and monitoring Lamb waves was effective in the detection and localization of a newly introduced damage. A different approach for damage detection in thin plates and aerospace structures via the use of electromechanical impedance was introduced by Giurgiutiu and Zagrai [39].

Kumar et al. [8] performed an in-situ Nondestructive evaluation (NDE) to monitor the health of fiber reinforced polymer (FRP) composite plate like structures. The research work employed Lamb wave transmission and reception with embedded piezoelectric wafer active sensors (PWAS). The SHM method was validated via experiments carried out on both isotropic and anisotropic plates.

A distinct transmissibility-based damage detection approach was proposed by Zhou et al. [40], making use of data acquired from Mahalanobis distance measurements when a beam was subjected to dynamic vibration. Kuang [5] introduced the monitoring of propagation of cracks and the detection of their locations in tubular steel specimens through the use of graded-index perfluorinated plastic optical fiber (GIPOF) coupled with a photon-counting optical time-domain reflector (OTDR). The optical fiber sensors have potential applications in monitoring the health of offshore steel structures.

Another common SHM method is the use of active guided ultrasonic waves in plate-like structures for damage detection[6]. Ultrasonic Guided Wave (UGW) method is in the category of nondestructive testing (NDT) techniques for damage detection especially in elongated structures such as pipelines and cylindrical bars. Zhang et al. [41] demonstrated the feasibility of detecting minor damage in pipe structures using guided wave signals and nonlinear oscillator. The proposed approach was verified using both theoretical modeling and experimental analysis, the results further emphasized the efficiency of the method even in the presence of significant noise effect and weak guided wave signals.

2.1.4 Samples of Theoretical Modelling and Simulation in Structural Health Monitoring

Technology is driven by the application of theories, laws, and principles. Theoretical modeling and simulation are usually used to verify the feasibility of experimental studies or complement the authenticity of results generated via experimental procedures. Researchers in SHM have resorted to the development of several theoretical models to validate the practical applications of their proposed techniques.

In a work done by Park et al. [42], an impedance-based real-time SHM technique with the capability of detecting multiple cracks in structures using PZT patches applied to concrete was presented. The researchers investigated the feasibility of its practical applications with a standard comparison of the analytical and experimental results. The analytical model used was based on a finite element model developed in ANSYS 6.0.

Huang and Kim [43] presented a numerical modeling of a smart composite laminate with single delamination at ply interface with an objective of probing its frequency response. The modal supposition method was used in calculating the frequency responses of the tip displacement and sensor outputs. The numerical modeling was based on an electromechanical coupled improved layerwise theory. The results confirmed a significant alteration on the dynamic characteristics of the composite when a delamination is introduced.

Delamination is a common damage form in structures and it is usually very difficult to handle because it inflicts internal injuries that can be barely seen via visual inspection. In a research work carried out by Lestari and Hanagud [44], the dynamic response of beams with multiple delaminations and its implication in the study of SHM in structures was thoroughly investigated. The numerical modeling was done using the Euler-Bernoulli beam theory and the results showed reasonable congruency with the experimental results.

In this research work, a theoretical model was developed using Euler Bernoulli beam theory to investigate the feasibility of detecting damage in a delaminated cantilever beam using a multipoint sensing coating.

2.2 Applications using piezoelectric composite materials

Sensors and actuators are used predominantly in the field of structural health monitoring. Most of these sensors are made of smart materials that possess piezoelectricity. Piezoelectricity is an intrinsic property of a material and its usefulness cannot be overemphasized.

2.2.1 Smart materials

In this present age of technological advancement, some substances fall into a special group with a common name called smart materials. Smart materials can be regarded as materials that receive, transmit, or process a stimulus and respond by producing a useful effect that may include a signal that the materials are acting upon. Smartness denotes self-adaptability, self-sensing, memory and multiple functionalities of the materials or structures [45]. The materials have a wide range of application in aerospace, manufacturing, biomechanics, and civil engineering.

In recent years, the world has experienced an increased leap in technology and it will be safe to call it the arrival of smart technology. It is a paradigm shift that comes with a focus on the possibilities of achieving faster and easier results to specified tasks through smart materials. Smart or intelligent materials are materials that have the intrinsic and extrinsic capabilities, first, to respond to stimuli and environmental changes and respond, to activate their functions according to these changes [46]. The best word which describes these materials that have increased sensitivity to external stimuli is "*smart*." Smart materials respond to external stimuli with quantifiable output signals.

The different types of Smart materials include Piezoelectric materials, Thermo-responsive materials, Magneto-restrictive materials, pH-sensitive materials, Chromogenic materials, and Polymer gels [45]. In terms of stimulus and response; piezoelectric materials receive stimulus in form of mechanical stress and give a response in units of electric charge, they have an inverse-piezoelectric effect that makes them undergo a mechanical strain when under the influence of an electric field. Electro-rheological fluids receive stimulus in the electric field and respond with a change in viscosity (internal damping). Magneto-restrictive material under the influence of a magnetic field experiences a mechanical strain. Shape memory alloys when heated change to their original memorized shapes. For optical fibers, changes in temperature, pressure and mechanical strain lead to changes in optoelectronic signals.

Smart materials are classified into two categories: active or passive [45]. Active smart materials are defined as materials which possess the capacity to modify their geometric or material properties under the application of electric, thermal or magnetic fields, thereby acquiring an inherent capacity to transduce energy. They include piezoelectric materials, shape memory alloys and magneto-restrictive materials. These active smart materials can be used as force transducers and actuators.

Passive smart materials lack the inherent capability to transduce energy. An example is fiber optic material. They can only be used as sensors and not actuators or transducers [45].

The uniqueness of piezoelectric materials has singled it out as a key player in this research work. These materials give an output of an electric charge when a mechanical force is applied, it also works in a reverse direction – undergoes a mechanical deformation when under the influence of an electric field. It offers an electromechanical effect. A piezoelectric material has mechanical properties - it obeys Hooke's law and has Young's Modulus. Simply put, mechanical stress on the piezoelectric material will initiate an electric charge that can be measured by an electrical device. When excited by an electric charge, it experiences a mechanical strain which could either be a compression or tension.

However, from the understanding of the piezoelectric constitutive form equation, some salient truths came to the fore. It must be noted that when a mechanical stress is applied on a piezoelectric material, it is expected to also show changes in its mechanical properties alongside the output of the electric charge. The same goes for the influence of the electric field, there is an electrical response alongside the evident mechanical deformation. There are different types of piezoelectric materials that have been used by various researchers for SHM applications.

The system to be employed for the effective sensitivity and acuity of piezoelectric material is explained as follows. A signal (mechanical in nature) must be sensed, processed and give an active feedback understandable by the monitors (humans). A sensor is required which collects the data, feeds the brain of the system (command and control unit) for processing and alerts the monitors through an actuator. It is important to recall that piezoelectric materials are active smart materials which mean they can be used as both sensors and actuators.

In the pool of published work on SHM applications, researchers used piezoelectric materials for data acquisition which was subsequently analyzed via different algorithms like neural networks and wavelet analysis. Islam and Craig [7] reported damage detection in composite structures with the use of piezoelectric materials trained with a neural network for response and data acquisition analysis. Yan and Yam [47] developed an online detection of damage in structures based on wavelet analysis using data generated from embedded piezoelectric materials.

Dib et al. [48] did a study which focused on the PZT ceramics as an in-situ structural health monitoring devices. Guided wave technique was used in measuring the health of the structure while impedance methods were used in monitoring the health of the PZT ceramic. It was concluded that the PZT will get good measurements and be in good conditions when they are 80 mm away from the point of impact which is a source of a potential damage.

Dziendzikowski et al. [49] carried out a comparative study on the use of embedded and surface mounted PZT transducers for barely visible impact damage detection and localization in composite structures. They found out that the electrical properties of PZT transducers are altered when embedded in composite structures but the sensitivity of the embedded transducers to damage can be greatly enhanced even after embedding. They, however, concluded that the capability of surface mounted PZT transducers in detection and location of barely visible impact damage surpassed that of their embedded counterparts.

Free naturally-occurring and manufactured piezoelectric materials include: quartz, tourmaline, lithium sulfate, Rochelle salt, Lead Zirconate Titanate (PZT), Poly Vinylidene Fluoride (PVDF), barium titanate ($BaTiO_3$) and zinc oxide (ZnO). In SHM applications, each of these materials exhibits different limitations. The choice of piezoelectric material is PZT ceramics because of its outstanding piezoelectric coefficient but is usually discarded in applications that require flexibility.

2.2.2 Applications using Zinc Oxide films and Poly Vinylidene Fluoride films

For SHM applications, the channels of instrumentation usually include systems that can measure physical quantities such as strain, displacement, and acceleration. These parameters can give detailed information about the health of the structures if properly analyzed via different methods. Strain sensors have been widely used in SHM applications. Piezoelectric materials can function as strain sensing devices.

Piezoelectric materials can be used as strain sensors either by bonding them to the surface or embedding them inside the host structure. Zinc Oxide is a wide gap semiconducting material that is electrically conductive with viable piezoelectric tendencies [50]. The ongoing in-depth research into the potential of zinc oxide reveals its wide range of applications in the industry and research advancements: gas sensors, solar cells, ceramics, biosensors, nano-generators, piezoelectric films, catalysts, nanostructures, and photodetectors [50]–[67].

The piezoelectric potential of zinc oxide was verified in a research conducted by Hu et al. [16]. The study introduced a flexible piezoelectric generator made of carbon nanotubes coated with zinc oxide delivered an average open-circuit voltage of 1.6V and short-circuit current of 75µA/cm^{-2}. The coating of the carbon nanotubes with zinc oxide was done using the atomic layer deposition (ALD).

Extensive studies involving SHM applications with piezoelectric materials have devised several means to bypass limitations encountered while using PZT ceramics by focusing on using zinc oxide. Taking a look at strides along applications using zinc oxide, Gullapalli et al. [12] fabricated a flexible strain sensor by embedding crystalline piezoelectric material (ZnO) in a flexible cellulose-based secondary matrix (paper). The nanocomposite material was made via a low-temperature solvothermal method which involved repeated soaking of the paper in a solution of zinc oxide crystals. Plasma sputtering was used for depositing two thin layers of gold coatings on the surface of the paper to serve as electrodes. The nanocomposite strain sensor yielded excellent strain sensitivity when tested under static and dynamic loadings.

A work done by Meyers et al. [10] was based on the findings of some researchers which validates that zinc oxide nanoparticles enhanced the remnant polarization and piezoelectricity of normal Poly (vinylidene fluoride-trifluoroethylene) (PVDF-TrFe) polymers. PVDF-TrFe is a piezoelectric polymer which is flexible and has recently gained recognition in SHM applications. The research work [10] characterized and validated Zinc Oxide/PVDF-TrFe Interdigitated Transducers (IDT) sensing and actuation performance. Firstly, a photolithography process was used for depositing an IDT electrode pattern on a Kapton substrate. Secondly, zinc oxide nanoparticles were suspended in a PVDF-TrFe solution using bath ultrasonication and then spin-coated on the IDT-Kapton substrate. The method of Lamb waves sensing and actuation validation testing was used to evaluate the damage detection capability of the substrate.

Studies that reveal the piezoelectric potential of zinc oxide for dynamic strain sensing include a research done by Loh and Chang [11]. The researchers succeeded in fabricating a piezoelectric thin film characterized with high piezoelectricity (excellent dynamic strain sensitivity) and favorable mechanical properties (stiff and flexible film conformable to different structural surfaces). The thin film was made via the dispersion of zinc oxide nanoparticles in polymers - poly (sodium 4-styrenesulfonate) (PSS) and poly (vinyl alcohol) (PVA) using high-energy probe sonication. The solvent for dispersing these particles was dried using solution evaporation. The experiment confirmed that optimum dynamic strain sensitivity and piezoelectricity was obtained at 50% and 60% ZnO-based films.

However, due to the low piezoelectric performance of zinc oxide films, some studies have shown that its piezoelectricity can be enhanced either via poling or by the addition of carbon nanotubes.

2.2.3 Applications involving the use of Carbon Nanotubes enhanced films

The alternative options of using zinc oxide, PVDF polymers and barium titanate for piezoelectric applications instead of PZT will yield tremendous success if their piezoelectric response can be enhanced or stimulated.

Carbon nanotubes have recently gained significant attention because of its extremely attractive properties such as high Young's modulus of elasticity, high aspect ratio, excellent stiffness, exceptional electrical conductivity and they are chemically stable [22],[23]. From theoretical calculations, Young's modulus of single walled carbon nanotubes (SWCNTs) ranges from 2.8 – 3.6 TPa and 1.7 – 2.4 TPa for multi-walled carbon nanotubes (MWCNTs) [70]. However, based on experimental evaluations, Young's modulus of SWCNTs and MWCNTs were described to be 1470 GPa and 950 GPa respectively [25],[26]. The electrical conductivity of individual MWCNTs was estimated to be between 20 and 2×10^7 S/m [73].

Since the outstanding discovery of carbon nanotubes in 1991 as reported by Iijima [74], there have been several applications that leverage its significant electrical and mechanical properties. Researchers have found amazing applications for CNTs [75] such as usage of composite materials, for enhancement of stiffness in coatings and films, for optimization of electrical performance in microelectronics, for increasing the capacity of lithium ion batteries and, used as components of biosensors.

A couple of researchers have investigated the possibility of using carbon nanotubes for the enhancement of the electromechanical response of piezoelectric materials. The carbon nanotubes were blended with the piezoelectric material and dispersed in polymers to fabricate piezoelectric films. Other films were developed as potential strain sensing devices by mixing carbon nanotubes with polymers.

Ramaratnam and Jalili [30] studied the influence of carbon nanotubes in the sensitivity of piezoelectric polymers using PVDF-TrFe polymer and two types of carbon nanotubes; Single Walled Carbon Nanotubes (SWCNT) and Multi-Walled Carbon Nanotubes (MWCNT). Experiments were conducted to evaluate the changes in the electromechanical responses of the three separate piezoelectric films fabricated; the plain PVDF-TrFe film, SWCNT-based film and MWCNT-based film. The carbon nanotube-based films yielded better piezoelectricity when compared to the plain PVDF-TrFe film while the SWCNT-based film produced responses greater than the MWCNT-based film. It was reported that the major improvement observed in the sensing capability of the piezoelectric polymers resulted from an increase in Young's modulus of elasticity of the nanotube-based polymer.

In other studies, carbon nanotubes were used in fabricating strain sensors usually by addition to a polymer to form a composite. Lee et al. [31] designed, fabricated and characterized spray-coated single-wall carbon nanotube film strain gauges. The prototype which was made by spray-coating SWCNT on a polyimide film with chromium plated electrodes was reported to show strain sensitivity approximately eight times greater than the commercial gauges. Multi-functional layer-by-layer carbon nanotube-polyelectrolyte thin films were proposed for strain and corrosion sensing by Loh et al. [32]. The polyelectrolyte-based thin films were produced from solutions of carbon nanotubes dispersed in poly (sodium 4-styrene-sulfonate) (PSS) and poly (vinyl alcohol) (PVA). The dispersion was facilitated via bath and probe sonication.

Kang et al. [76] developed a carbon nanotube strain sensor suitable for SHM applications by dispersing SWCNTs in poly methyl methacrylate (PMMA). The usage of poly (methyl methacrylate) (PMMA) was further explored by Pham et al. [77] in the fabrication of a conductive polymeric composite film. The composite was made via either melt-processing or solution casting of the polymer matrices containing low concentrations of multi-walled carbon nanotubes (MWCNTs). The developed thermoplastic/carbon nanotube films were proposed for strain sensing applications.

Anand and Mahapatra [33] developed thin films by dispersing carbon black nanoparticles and carbon nanotubes in an epoxy polymer. Several concentrations of MWCNTs in the carbon black and epoxy matrix were considered, such as 0.142%, 0.285%, 0.57%, 0.855% and 1.14% by weight. The best concentration of MWCNTs in the epoxy matrix with high sensitivity while under static mechanical loading was recorded at 0.57%. The thin film has potential applications to be used as strain sensors and accelerometers which are heavily used by experts in SHM.

Furthermore, in a study to investigate the impact of both multi-walled carbon nanotubes and graphene platelets (GnPs) in a three-phase nanocomposite containing PZT and epoxy, the fabricated nanocomposites were subjected to electrical and mechanical tests. Saber et al. [78] revealed that GnPs increased the poling behavior and dynamic response of the composites (PZT and epoxy) which yielded better results when compared to ones with MWCNTs. This research opened the path for the use of GnPs as prospective materials for enhancing the piezoelectric response of nanocomposites targeted for SHM applications.

2.3 Methods of Fabrication of Nanocomposites

In the fabrication of nanocomposites, two or more materials with varying weight percentages are mixed together using different techniques which are usually dependent on the polymer type used.

Materials that make up the nanocomposites are usually carbon nanotubes, polymers, and piezoelectric materials. The homogeneity of composites depends largely on the methods of mixing and other fabrication procedures.

The piezoelectric performance of nanocomposites is affected by three key factors[20]: the interfacial bonding between the polymer and the main constituent materials, the alignment of the piezoelectric particles in the polymeric matrix and the homogeneity in the dispersion of the piezoelectric particles in the composite. All these factors are needed for a seamless load transfer and charge generation in the nanocomposites.

2.3.1 Solvent Casting

Solvent casting is the most common method used in the fabrication of nanocomposites though it is dependent on the solubility of the constituent materials. Solvent casting is highly desirable because it stimulates nanotube dispersion and homogeneity of the composite via energetic agitation. This agitation is usually achieved by magnetic stirring, reflux, shear mixing, or commonly via sonication. Sonication is carried out either through a mild sonication in a bath or a high-power sonication using a tip or horn.

This method starts with a dispersion of carbon nanotubes, a piezoelectric material, a polymer in a solvent, all added together and mixed vigorously for a specific period. The solvents commonly used in the fabrication process are water, ethanol, and Dimethyl Formamide (DMF). After the mixture of the constituents to form a homogenous solution, the solution is applied on layers in a way that films can be manufactured after the evaporation of the solvent. The solidification of the nanocomposite films can be aided via any means that quickens the evaporation of the solvent.

A sizeable number of research work showing the production of CNT/polymer nanocomposites through the solvent casting method has been published [18][19]. Benoit et al. [18] dispersed PMMA and SWCNTs in toluene. The resulting solution after sonication was used for making electrically conductive composite films by drop casting the solution on a glass substrate. Mathur et al. [19] reported the analysis of MWCNTs-reinforced composites with enhanced electrical and mechanical properties. Two separate solutions were made from sonication of MWCNTs/polystyrene (PS)/toluene and MWCNTs/polymethyl methacrylate (PMMA)/toluene. The conductive thermoplastics were fabricated using the solvent casting technique with potential applications for Electromagnetic Interference (EMI) shielding. In a related research, Shaffer and Windle [79] fabricated a MWCNT-based composite film by dispersing MWCNTs in water and mixed the solution with a solution of Poly Vinyl Alcohol (PVA) in water.

2.3.2 Melt Mixing

Another commonly used method in mixing materials for the fabrication of nanocomposites is called melt mixing. This is generally used for composites involving thermoplastics because these polymers undergo a reduction in hardness when heated. This technique uses high temperatures to initiate a decrease in viscosity of substrates and high shear forces to upset the nanotubes bundle. Nanocomposites of different sizes are fabricated using methods such as compression molding, injection molding or extrusion. [20] Andrews et al. [80] investigated the fabrication of nanocomposite fibers and thin films made of MWCNTs and industrial polymers such as polystyrene, polypropylene, and acrylonitrile-butadiene-styrene (ABS) via melt processing. The dispersion of carbon nanotubes in these polymers was done under the impact of high shear forces and elevated temperatures. Compression molding was used to form thin composite films. Other researchers also studied the processing of nanocomposites using shear mixing and compression molding.[29]

Asides solvent casting and melt mixing, other methods employed in the production of nanocomposites include in-situ polymerization [22][23], twin screw pulverization [24], latex fabrication [25][26], coagulation spinning [27] and electrophoretic deposition [28].

Other researchers fabricated nanocomposites of carbon nanotubes by combining two or more of the techniques discussed above. In a research carried out by Singh et al. [81] to investigate the use of nanocomposites for the suppression of electromagnetic radiation, MWCNT reinforced Low-density polyethylene (LDPE) were fabricated via solvent casting which was followed by compression molding. In the synthesis and characterization of MWCNT-polymethyl methacrylate composites (MWCNT-PMMA), Pande et al. [81] used in-situ polymerization combined with compression molding.

From the literature review, researchers have proposed the fabrication of piezoelectric sensors with SHM applications but there are certain limitations in their usage. The nanocomposites fabricated were made in form of films but can only be attached to a single point on the surface of the structure with the smooth surface condition. The limitations also include complex and expensive fabrication techniques.

In this research work, special attention is given to the fabrication of a piezoelectric nanocomposite paint that can be used for damage detection and strain sensing in structures. The aim is to investigate the possibility of realizing multi-point sensing and fabricate piezoelectric sensors that can cover a large surface area without using highly complicated methods. The objective of this research is to produce a piezoelectric nanocomposite paint that can be optimized for strain sensing applications in structures. The paint is expected to bond strongly to the various surface conditions of the engineering structure and exhibit excellent mechanical properties.

Chapter 3 Theoretical Model and Methodology

In this chapter, the theoretical models and simulations for exploring the feasibility of damage detection techniques with the use of a piezoelectric paint are discussed. The simulation is carried out using MATLAB code and the results of the theoretical modeling are also discussed in detail.

The essence of the theoretical model is to simulate a damage detection technique that can possibly be realized with the application of the nanocomposite paint that is produced in chapter 4 of this research work. Instead of the nanocomposite paint, a PZT coating applied to the surface of a delaminated cantilever beam was used in the simulation.

The damage detection technique used in the delaminated cantilever beam is through a piezoelectric coating attached to the surface of the beam. When the beam is subjected to harmonic loading, the alteration in the voltage generated by the piezoelectric patch across the whole length of the beam is observed at different time points.

The theoretical model developed will be used for the calculation of the natural frequencies, and mode shapes of the delaminated cantilever beam. The voltage generated by the piezoelectric coating will also be calculated when a harmonic load is applied on its tip at the free end.

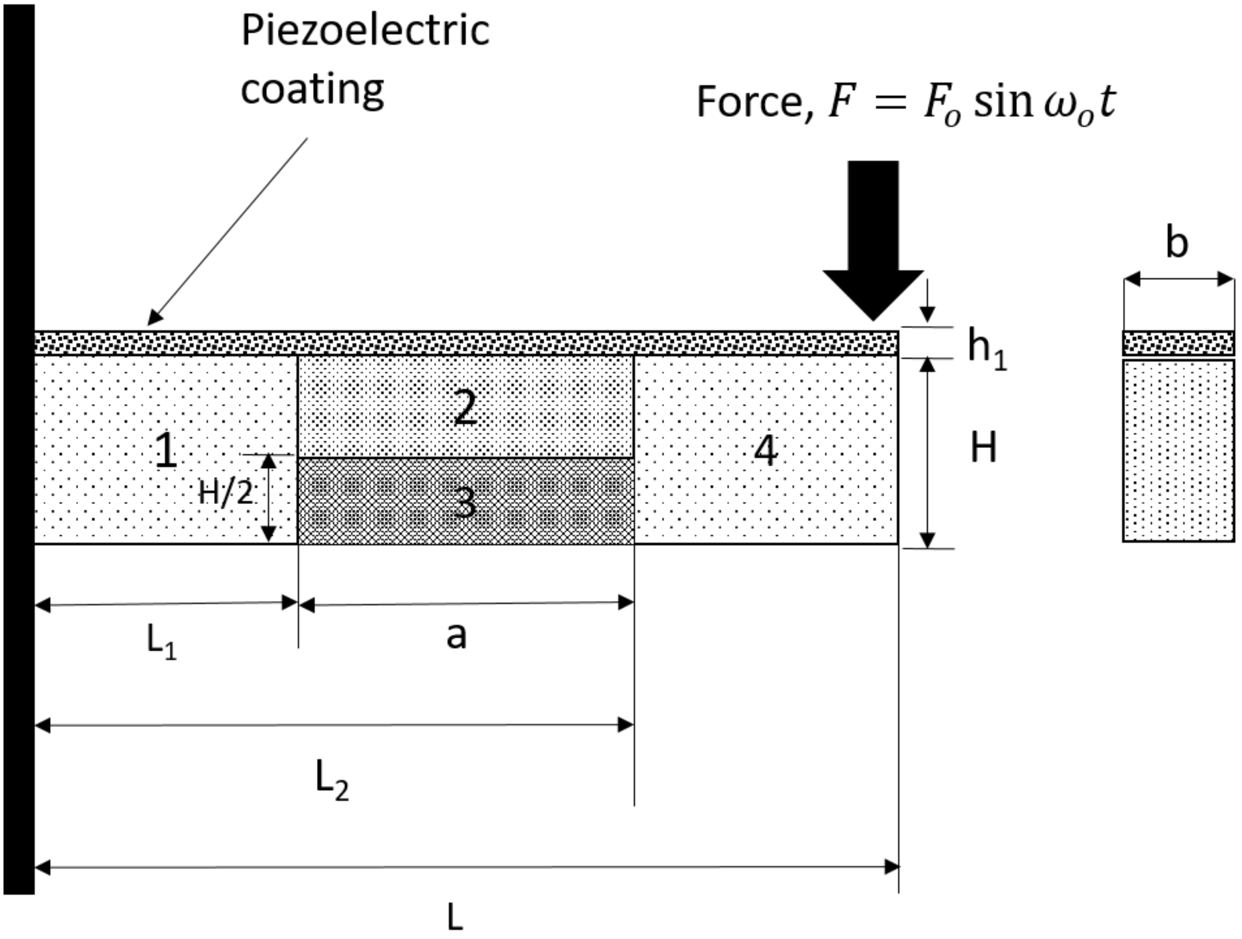

Figure 3-1: A schematic diagram of a delaminated cantilever beam with the piezoelectric coating subjected to a point load

3.1 Calculation of the natural frequencies, mode shapes, and deflection

The delaminated cantilever beam with the piezoelectric coating attached to the upper surface is shown in Figure 3.1. The geometric dimensions of the beam are given as; length, L, width, b and height or thickness, H. The piezoelectric coating has the same length, L, and width, b as with the beam but with thickness, h_1 and it covers the whole surface. The areas labeled 2 and 3 are the areas of delamination, they are both of length, a, with each of them having a height, H/2, and the same width, b. The distances from the fixed end of the beam to the right and left ends of the delaminated section are L$_1$ and L$_2$, respectively. The harmonic load applied at the tip of the beam to calculate deflection is given as; $F = F_o \sin \omega_o t$, where ω_o is the angular frequency of the applied force with F$_o$ as its amplitude.

The theoretical model is based on the governing equations from Euler-Bernoulli Theory of beams;

$$M(x) = EI(x)\frac{d^2w}{dx^2} \qquad (3 - 1)$$

Where M(x) is known as the bending moment, E is Young's modulus and I is the moment of inertia of the body involved. The assumption for the Euler Bernoulli beam theory states that after bending there is a new position; there is no relative deformation between two close points in the same cross-section on the beam. However, Euler's assumption is only valid for very small deflections in beams.

For full forced vibration analysis, the governing equation based on the Euler-Bernoulli theory is given as:

$$EI(x)\frac{d^4w(x,t)}{dx^4} + pA\frac{\partial^2 w(x,t)}{\partial x^2} = f(x,t) \qquad (3 - 2)$$

The beam is separated into four different sections where W$_1$, W$_2$, W$_3$, and W$_4$ are the amplitudes of the modal functions of the first, second, third and fourth sections of the beam respectively.

The free vibration solutions of the delaminated beam can be given as:

$$W_1 = C_1 \cos k_1x + C_2 \sin k_1x + C_3 \cosh k_1x + C_4 \sinh k_1x \qquad (0 \le x \le L_1) \qquad (3 - 3)$$

$$W_2 = C_5 \cos k_2x + C_6 \sin k_2x + C_7 \cosh k_2x + C_8 \sinh k_2x \qquad (L_1 \le x \le L_2) \qquad (3 - 4)$$

$$W_3 = C_9 \cos k_3x + C_{10} \sin k_3x + C_{11} \cosh k_3x + C_{12} \sinh k_4x \qquad (L_1 \leq x \leq L_2) \qquad (3 - 5)$$

$$W_4 = C_{13} \cos k_1x + C_{14} \sin k_1x + C_{15} \cosh k_1x + C_{16} \sinh k_1x \qquad (L_2 \leq x \leq L) \qquad (3 - 6)$$

where C_1 to C_{16} are unknown constants and k_1 to k_3 are given as

$$k_1^4 = \frac{pA_1\omega^2}{EI_1}$$

$$k_2^4 = \frac{pA_2\omega^2}{EI_2}$$

$$k_3^4 = \frac{pA_3\omega^2}{EI_3} \qquad (3 - 7)$$

3.2 Boundary Conditions

Whenever a damage or delamination occurs in a system or structure, there is a change in the continuity of the structural response, which can be observed as changes in the natural frequencies and mode shapes. Because of the delamination in the cantilever beam under study, there is a difference in the dynamic characteristics of each of the sections which are visible from the alteration of their physical properties. The delamination, in this case, has resulted in the generation of 16 boundary conditions at x = 0, L_1, L_2 and L describing the structural continuity.

The boundary conditions are given below:

At x = 0 (at the fixed end)

$$W_1 = 0$$

$$\frac{dW_1(x)}{dx} = 0 \tag{3 - 8}$$

At x = L1 (at the beginning of the delamination length)

$$W_1(x) = W_2(x)$$

$$W_1(x) = W_3(x)$$

$$\frac{dW_1(x)}{dx} = \frac{dW_2(x)}{dx}$$

$$\frac{dW_1(x)}{dx} = \frac{dW_3(x)}{dx}$$

$$EI_1 \frac{d^2W_1(x)}{dx^2} = EI_2 \frac{d^2W_2(x)}{dx^2} + EI_3 \frac{d^2W_3(x)}{dx^2}$$

$$EI_1 \frac{d^3W_1(x)}{dx^3} = EI_2 \frac{d^3W_2(x)}{dx^3} + EI_3 \frac{d^3W_3(x)}{dx^3} \tag{3 - 9}$$

At x = L2 (at the end of the delamination length)

$$W_2(x) = W_4(x)$$

$$W_3(x) = W_4(x)$$

$$\frac{dW_2(x)}{dx} = \frac{dW_4(x)}{dx}$$

$$\frac{dW_3(x)}{dx} = \frac{dW_4(x)}{dx}$$

$$EI_2 \frac{d^2W_2(x)}{dx^2} + EI_3 \frac{d^2W_3(x)}{dx^2} = EI_1 \frac{d^2W_4(x)}{dx^2}$$

$$EI_2 \frac{d^3W_2(x)}{dx^3} + EI_3 \frac{d^3W_3(x)}{dx^3} = EI_1 \frac{d^3W_4(x)}{dx^3} \tag{3 - 10}$$

At x = L (at the free end)

Shear force (Q) = $EI_1 \frac{d^3W_4(x)}{dx^3}$ = 0

Bending Moment (M) = $EI_1 \frac{d^2W_4(x)}{dx^2}$ = 0 (3 - 11)

Putting equations (3-3), (3-4), (3-5), and (3-6) into the boundary conditions of the delaminated cantilever beam, equations (3-8), (3-9), (3-10) and (3-11) leads to 16 linear equations.

$$\begin{bmatrix} C_1 \\ \vdots \\ C_{16} \end{bmatrix} [K_i - m\omega^2] = \begin{bmatrix} 0 \\ \vdots \\ 0 \end{bmatrix} \quad (3 - 12)$$

The 16 linear equations are listed as follows:

$$C_1 = 0 \quad (3 – 13a)$$

$$-k_1 C_1 \sin k_1 x + k_1 C_2 \cos k_1 x + k_1 C_3 \sinh k_1 x + k_1 C_4 \cosh k_1 x = 0 \quad (3 – 13b)$$

$$C_1 \cos k_1 L_1 + C_2 \sin k_1 L_1 + C_3 \cosh k_1 L_1 + C_4 \sinh k_1 L_1 - C_5 - C_7 + \cdots = 0 \quad (3 – 13c)$$

$$C_1 \cos k_1 L_1 + C_2 \sin k_1 L_1 + C_3 \cosh k_1 L_1 + C_4 \sinh k_1 L_1 - C_9 - C_{11} + \cdots = 0 \quad (3 – 13d)$$

$$-k_1 C_1 \sin k_1 L_1 + k_1 C_2 \cos k_1 L_1 + k_1 C_3 \sinh k_1 L_1 + k_1 C_4 \cosh k_1 L_1 - k_2 C_6 - k_2 C_8 + \cdots = 0$$

(3 – 13e)

$$-k_1 C_1 \sin k_1 L_1 + k_1 C_2 \cos k_1 L_1 + k_1 C_3 \sinh k_1 L_1 + k_1 C_4 \cosh k_1 L_1 - k_3 C_{10} - k_3 C_{12} = 0$$

(3 – 13f)

$$-EI_1 k_1^2 C_1 \cos k_1 L_1 - EI_1 k_1^2 C_2 \sin k_1 L_1 + EI_1 k_1^2 C_3 \cosh k_1 L_1 + EI_1 k_1^2 C_4 \sinh k_1 L_1 + EI_2 k_2^2 C_5 - EI_2 k_2^2 C_7 + EI_3 k_3^2 C_9 - EI_3 k_3^2 C_{11} = 0 \quad (3 – 13g)$$

$EI_1k_1^3C_1\sin k_1L_1 - EI_1k_1^3C_2\cos k_1L_1 + EI_1k_1^3C_3\sinh k_1L_1 + EI_1k_1^3C_4\cosh k_1L_1 + EI_2k_2^3\,C_6 -$

$EI_2k_2^3C_8 + EI_3k_3^3C_{10} - EI_3k_3^3C_{12} = 0$ (3 – 13h)

$C_5\cos k_2a + C_6\sin k_2a + C_7\cosh k_2a + C_8\sinh k_2a - C_{13} - C_{15} = 0$ (3 – 13i)

$C_9\cos k_3a + C_{10}\sin k_3a + C_{11}\cosh k_3a + C_{12}\sinh k_3a - C_{13} - C_{15} = 0$ (3 – 13j)

$-k_2C_5\sin k_2a - k_2C_6\cos k_2a + k_2C_7\sinh k_2a + k_2C_8\cosh k_2a - k_1C_{14} - k_1C_{16} = 0$

(3 – 13k)

$-k_3C_9\sin k_3a - k_3C_{10}\cos k_3a + k_3C_{11}\sinh k_3a + k_3C_{12}\cosh k_3a - k_1C_{14} - k_1C_{16} = 0$

(3 – 13l)

$-EI_2k_2^2C_5\cos k_2a - EI_2k_2^2C_6\sin k_2a + EI_2k_2^2C_7\cosh k_2a + EI_2k_2^2C_8\sinh k_2a -$

$EI_3k_3^2C_9\cos k_3a - EI_3k_3^2C_{10}\sin k_2a + EI_3k_3^2C_{11}\cosh k_3a + EI_3k_3^2C_{12}\sinh k_3a +$

$EI_1k_1^2\,C_{13} - EI_1k_1^2C_{15} = 0$ (3 – 13m)

$EI_2k_2^3C_5\sin k_2a - EI_2k_2^3C_6\cos k_2a + EI_2k_2^3C_7\sinh k_2a + EI_2k_2^3C_8\cosh k_2a +$

$EI_3k_3^3C_9\sin k_3a - EI_3k_3^2C_{10}\cos k_3a + EI_3k_3^3C_{11}\sinh k_3a + EI_3k_3^3C_{12}\cosh k_3a +$

$EI_1k_1^3\,C_{14} - EI_1k_1^3C_{16} = 0$ (3 – 13n)

$EI_1k_1^3C_{13}\sin k_1L - EI_1k_1^3C_{14}\cos k_2L + EI_1k_1^3C_{15}\sinh k_2L + EI_1k_1^3C_{16}\cosh k_2L = 0$ (3 – 13o)

The 16 linear equations are solved using MATLAB to determine the angular natural frequencies in the first three modes of free vibration, the unknown constants, C_1 to C_{16} are calculated in a bid to get the nth solutions of the normal modal expression of the beam. The code for the solution is provided in Appendix A.

Table 3-1. Material properties of the stainless-steel beam and the piezoelectric coating

Parameters	**Host beam (Steel)**	**Piezoelectric coating (PZT4)**
L(m)	1.0	
L_1(m)	0.3	
a(m)	0.4	
L_2(m)	0.7	
b(m)	0.05	0.013
H(m)	0.001	
h_1(m)		0.0003
Young's modulus, E (Nm^{-2})	200×10^9	
Mass density, ρ (kgm^{-3})	8×10^3	7.5×10^3
e_{31} (Cm^{-2})		-2.8
C_v (nF)		0.75 for the piezoelectric coating with the geometry of 0.01, 0.06, 0.003m

3.3 Results

The mode shapes of the free vibration of the delaminated cantilever beam bonded with a piezoelectric coating are shown in Figure 3.2 to Figure 3.4. These mode shapes show clearly that there is a difference in the dynamic responses of a healthy and an unhealthy cantilever beam due to the introduction of delamination.

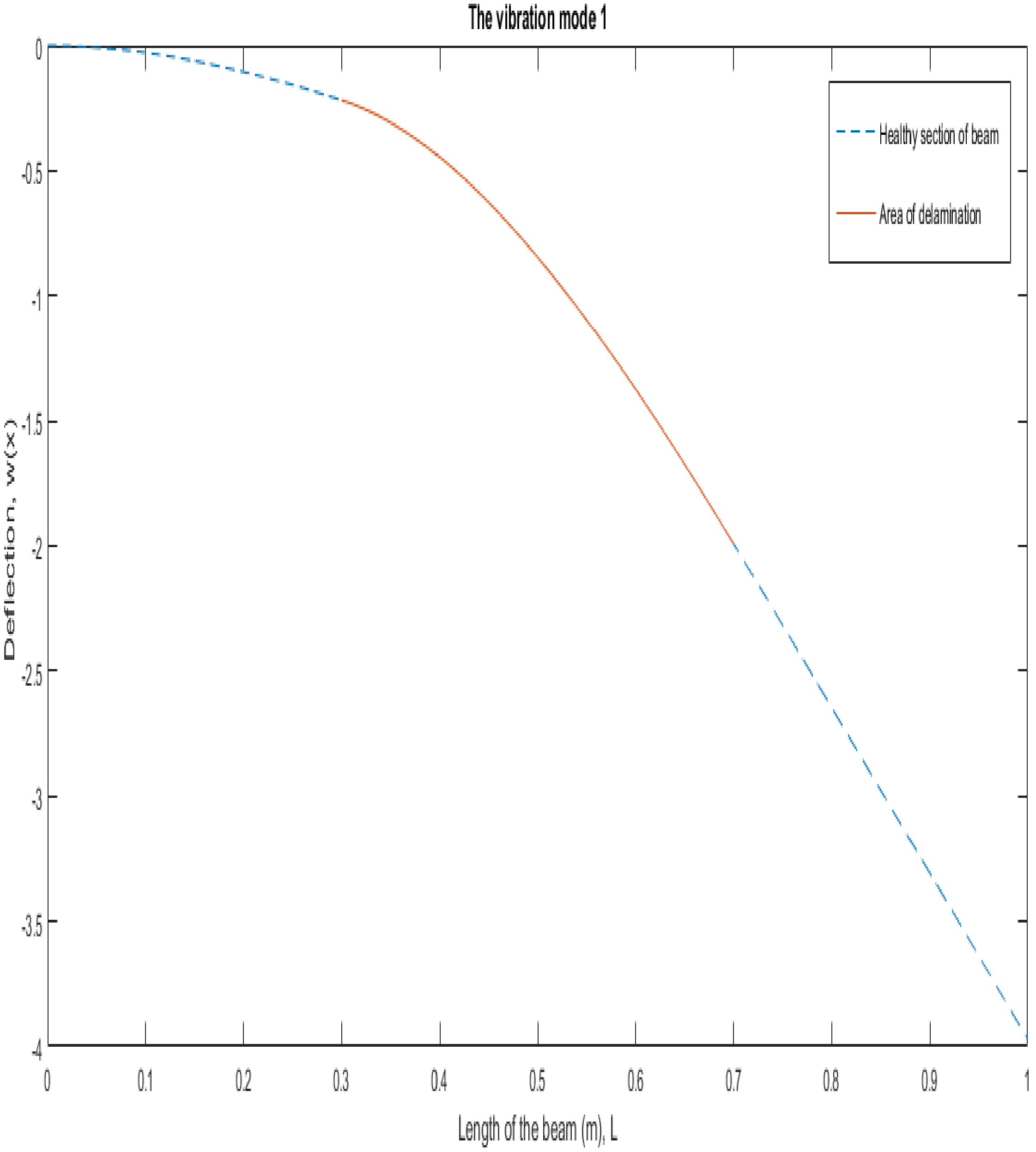

Figure 3-2: The first mode shape

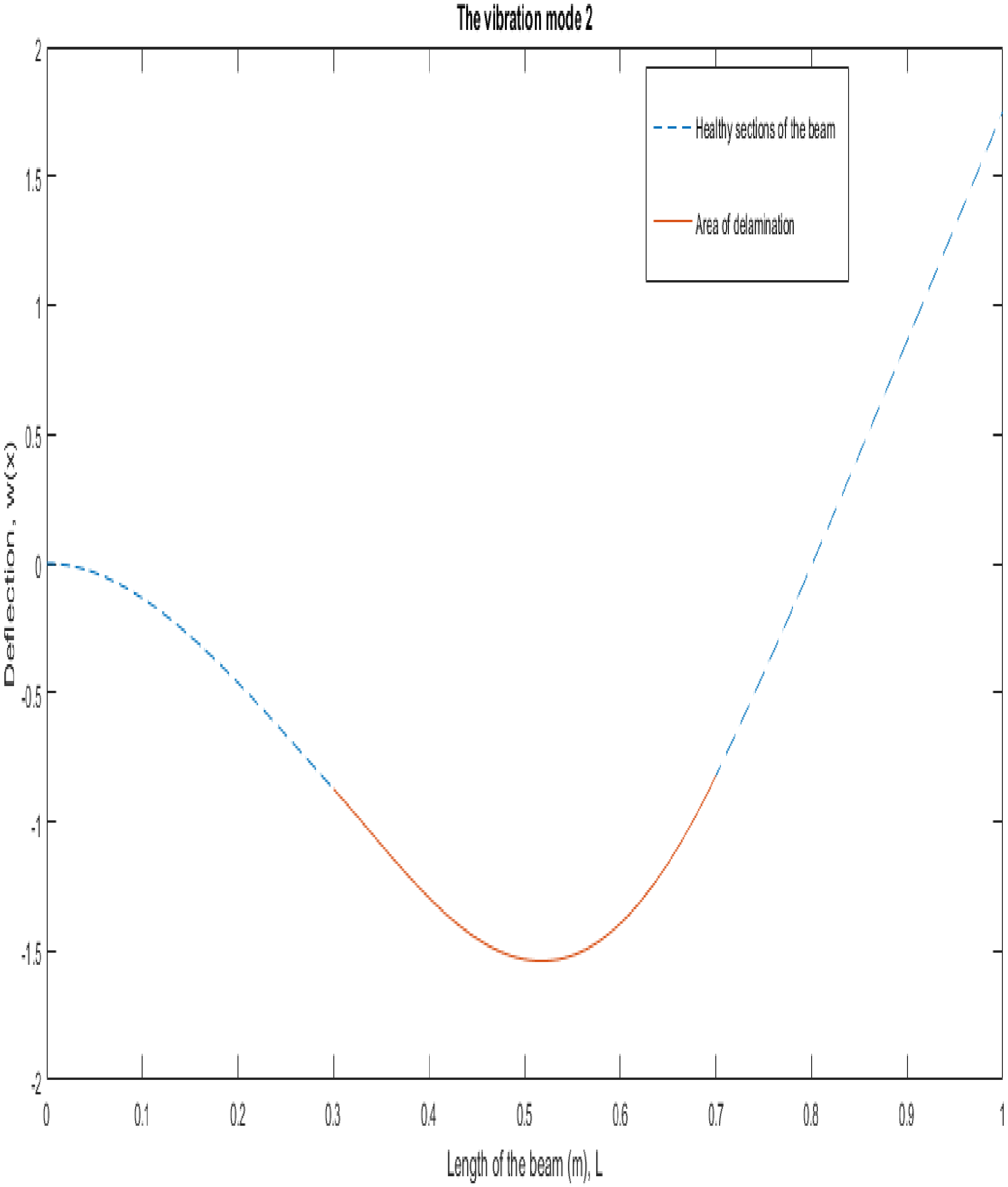

Figure 3-3: The second mode shape.

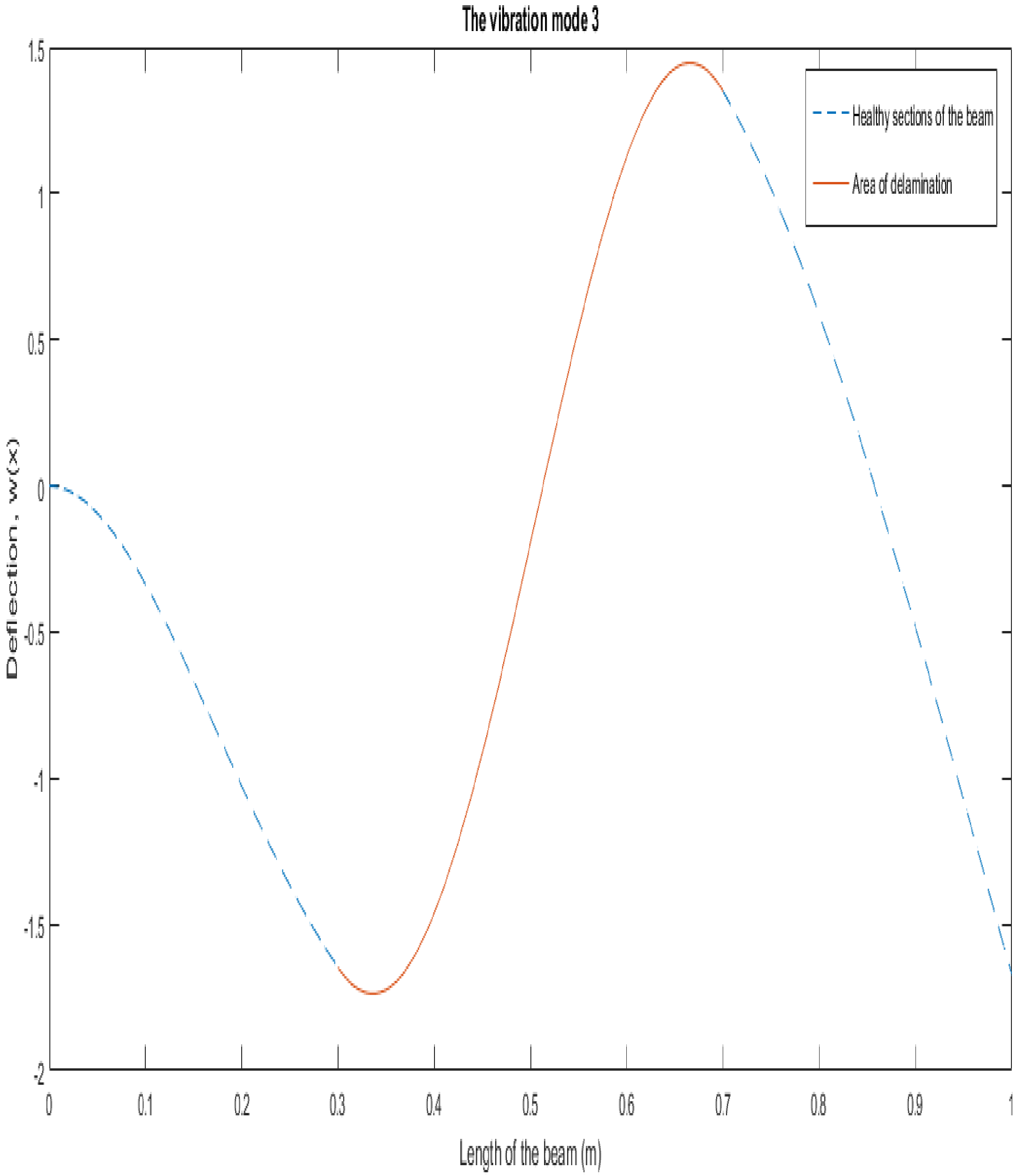

Figure 3-4: The third mode shape.

Using the principle of mode superposition. The deflection of the beam is assumed as:

$$w(x,t) = \sum_{n=1}^{\infty} W_n(x).\, q_n(t) \tag{3 - 14}$$

Where $W_n(x) = sum\ of\ nth\ mode\ shapes$ and for steady state vibration from a forcing function

$$q_n(t) = \frac{1}{pAbw_n} \int_0^t Q_n(\tau) \sin \omega_n (t - \tau) d\tau \tag{3 - 15}$$

$$b = \int_0^l W_n^2(x) dx \tag{3 - 16}$$

$$Q_n(t) = \int_0^l f(x,t)\, W_n(x) dx \tag{3 - 17}$$

Putting equations (3-15), (3-16) and (3-17) in equation (3-14) lead to the solution which yielded the deflection of the beam from n =1 t͠o 4. The deflection of the delaminated cantilever beam with the bonded piezoelectric coating was calculated after a force, $F = F_o \sin \omega_o t$ was applied at its tip; where $F_o = 10N$ and $\omega_o = 30rad/s$. The deflection curves of the beam at different time points due to the dynamic harmonic loading are shown in Figure 3.5.

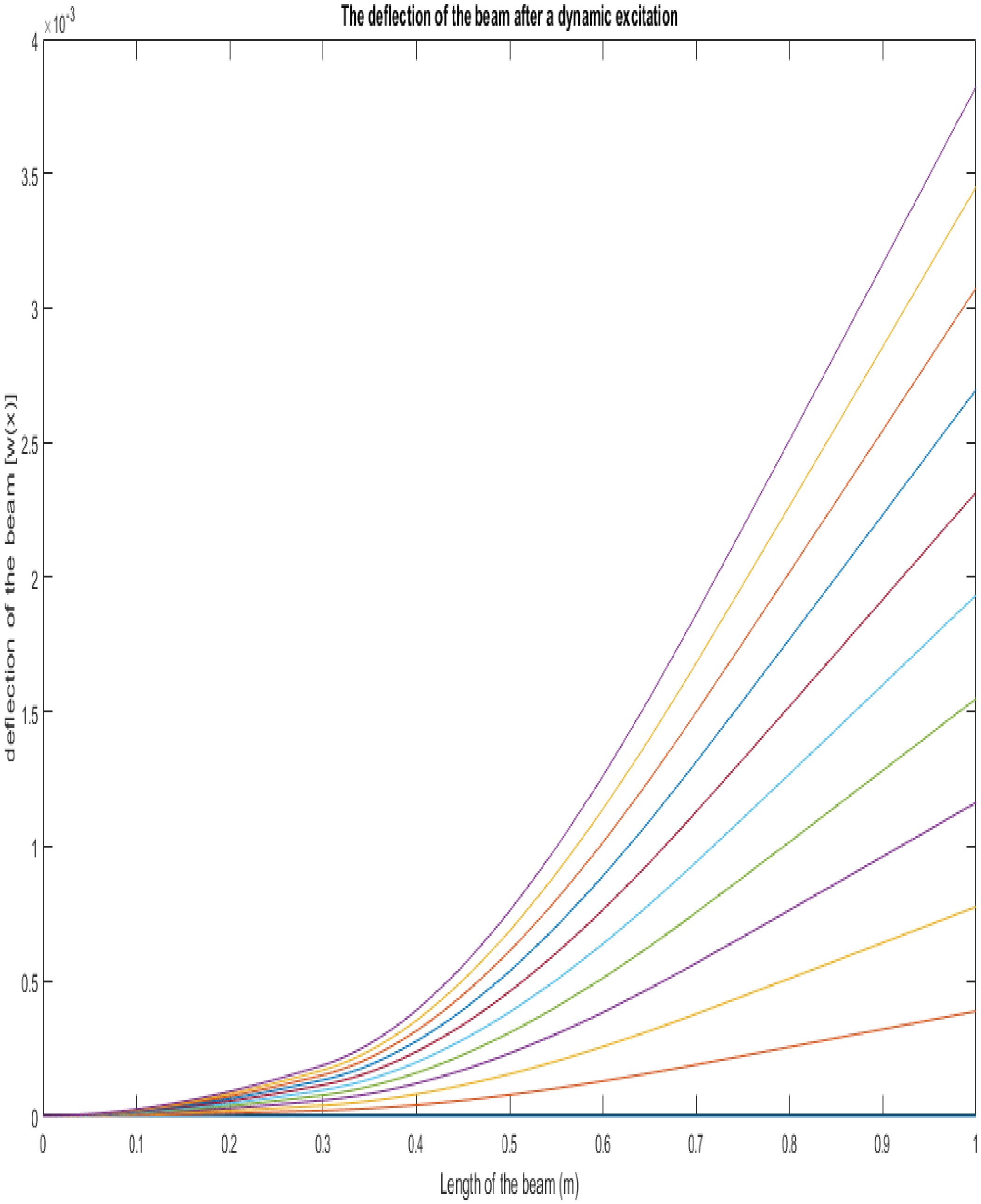

Figure 3-5: The dynamic deflection of the delaminated cantilever beam bonded with a piezoelectric coating after a harmonic load was applied at the tip of the free end.

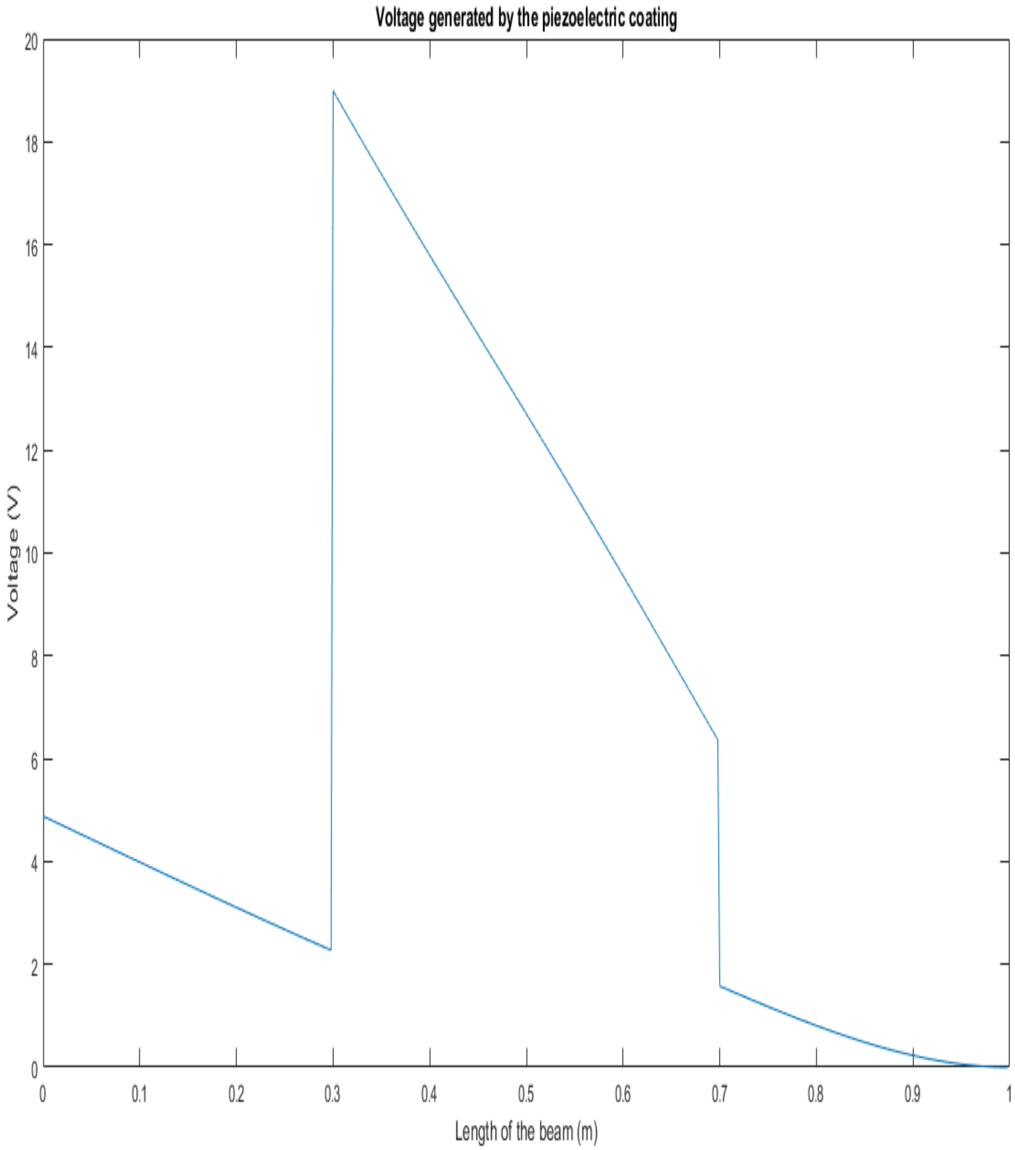

Figure 3-6: The Voltage distribution across the whole length of the beam showing a discontinuity in the section of delamination (from L_1 = 0.3m to L_2 = 0.7m).

3.4 Voltage generation from the piezoelectric coating

From the deflection of the beam, the curvature of the beam was calculated at different time points.

$$w(x,t) = \sum_{n=1}^{\infty} W_n(x).\, q_n(t)$$

Where $W_n(x) = sum\ of\ nth\ mode\ shapes$

$$\text{Curvature} = \frac{d^2 w(x,t)}{dx^2} \qquad (3 - 18)$$

The electrical charge generated on the surface of the piezoelectric coating at different position x_l with small section length of Δl is given as,

$$Q(x_l) \ = -e_{31} \int_l^{l+\Delta l} b \left(\frac{H+h_1}{2}\right) \frac{d^2 w}{dx^2}\ dx\ (0<x_l<L) \qquad (3 - 19)$$

$-e_{31}$ is the piezoelectric constant, b is the width of the beam, H is the thickness of the beam, h_1 is the thickness of the piezoelectric coating and w is the deflection of the host beam.

The voltage generated, V from the piezoelectric coating is given as:

$$V(x_l) = \frac{Q}{C_v} = \ -e_{31} \frac{(H+h_1)}{2C_v} \left(\frac{dw(x,t)}{dx} |at\ x_{=x_l+\Delta l} - \ \frac{dw(x,t)}{dx} |at\ x_{=x_l} \right) (3 - 20)$$

The sharp discontinuity in the voltage distribution along the length of the beam as observed in Figure 3.6 validates the damage detection and location via the piezoelectric coating attached to the top surface of the beam. In the theoretical modeling, delamination in the form of damage introduced in the cantilever beam altered the boundary conditions, the dynamic characteristics of the beam. At the beginning of the delamination, a discontinuity in the curvature distribution of the beam which is a function of the voltage generated by the piezoelectric coating. This simulation shows the feasibility of having a piezoelectric coating capable of multipoint strain sensing. It is possible to use the nanocomposite smart paint produced in Chapter 4 as a form of damage detection sensor.

Chapter 4 Production and Characterization of Nanocomposite Smart Paint

This chapter describes the steps involved the production of the nanocomposite smart paint with vivid explanations of the major processes employed. It also summarizes the procedures used in the characterization of the electrical, mechanical and microstructural properties of the paint. All the practical methods for the fabrication and characterization of the nanocomposite paint are discussed.

4.1 Experimental Details

For the fabrication of the piezoelectric nanocomposite paint, several methods are explored using the key materials.

4.1.1 Materials

The materials used for the production of the piezoelectric nanocomposite paint include zinc oxide (ZnO) nanopowder dispersion in water, Multi-Walled Carbon Nanotubes dispersion in water (MWCNTs), Poly Vinyl Acetate (PVA) glue and Steel beam. The specific physical and chemical properties of the key chemicals used alongside their sources are shown in Table 4.1.

Table 4-1: The specific physical and chemical properties of some chemicals used in the fabrication of the nano-composite paint.

Name	**Properties**	**Source**
Poly Vinyl Acetate (PVA glue)	Soluble in water	Books by Hand ®
Multi-Walled Carbon Nanotubes (MWCNTs) in water dispersion	3wt%, >95+%, OD: 5-15 nm, ID: 3-5 nm, length: 50 µm	US Research Nanomaterials. Inc., Houston, Texas, United States of America.
Zinc Oxide nanoparticles dispersion in water (ZnO)	<100 nm particle size (DLS), <35 nm avg. part size (APS), 50 wt.% in water)	Sigma Aldrich®, St. Louis, Missouri, United States of America.

4.2 Production of Piezoelectric Nanocomposite Paint

Carbon Nanotubes (CNTs), PVA glue and zinc oxide nanoparticles dispersion make up the formation of the nanocomposite paint solution. Mixing these materials to form a homogeneous composite is affected by numerous factors. In the fabrication of nanocomposites, two or more materials in varying percentages are mixed together using different techniques which are usually dependent on the polymer type used and the dispersal medium. In this research work, the mixing methods employed are magnetic stirring, manual mixing, and sonication.

4.2.1 Preparation of homogeneous nanocomposite paint

To achieve better homogeneity in the nano-composite paint, the mixing method and method of deposition of the solution on the metal surface were altered. Asides sonication, magnetic stirring, and manual mixing methods are explored for the formation of a homogeneous solution.

Unexpectedly, these two methods produced paints replete with numerous cracks and pores as shown in Figure 4.1 and it also yielded insignificant amount of piezoelectricity when tested during calibration. The pores and cracks in the coating shown in Figure 4.1 are because of the numerous bubbles that are formed in the nanocomposite solution during these mixing methods. The bubbles form the cracks in the dried-out coating.

Spin coating method was used for applying the mixed solution on a metal substrate since spin coating aids uniform deposition. Unfortunately, the samples made from spin coating did not yield tangible amount of piezoelectricity because of the very thin layers that were formed. The spin coating was carried out on the samples with a speed of 2000 rpm, a ramp speed of 600 rpm, all for 10 seconds.

8ml of zinc Oxide nanoparticles dispersion (< 100 nm particle size, <35 nm avg. part size with a concentration of 50 wt.% in water) and varying amounts of CNTs solution (3 wt.%, >95+%, OD: 5-15 nm, ID: 3-5 nm, length 50 µm) are added to 2 ml of PVA glue, all in a centrifuge tube. The three liquids are mixed via sonication by using the high-energy probe ultrasonic mixer for two hours. Lu et al. [82] reported the possibility of rupture of CNTs and alterations in its aspect ratio as the adverse effects of prolonged sonication of CNTs during their dispersion in liquids. Study of other similar research work that involved the ultrasonic mixing of CNTs agreed on two hours as the optimum time for sonication. The sonication approach produces a relatively homogeneous solution after failed attempts to get a uniform solution via magnetic stirring and manual mixing. The solvent casting method is used to produce different nanocomposite paints.

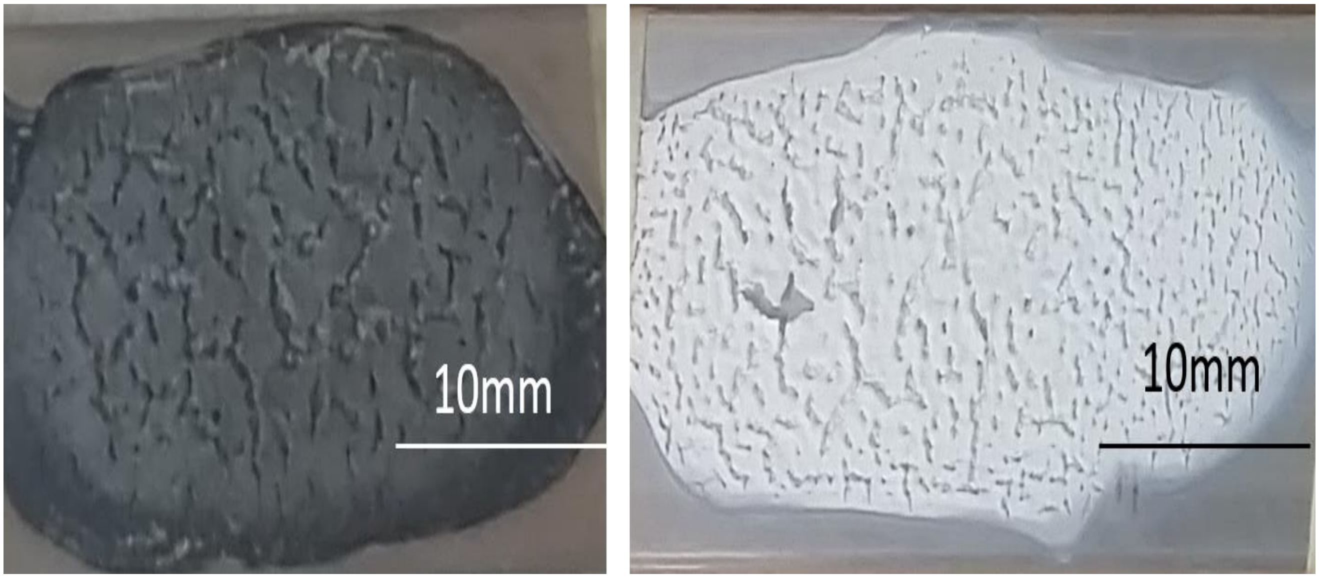

Figure 4-1: The paint with many cracks and voids was made from nanocomposite solution produced via magnetic stirrer.

Step 1: Five samples of solutions are produced based on varying compositions (% by weight) of the three main constituents: zinc oxide nanoparticles dispersion, PVA glue, Multi-walled Carbon nanotubes. Compositions of different materials in different samples are given in Figure 4.2. These different samples were produced to investigate the effect of the addition of CNTs on the material properties of the nanocomposite coating.

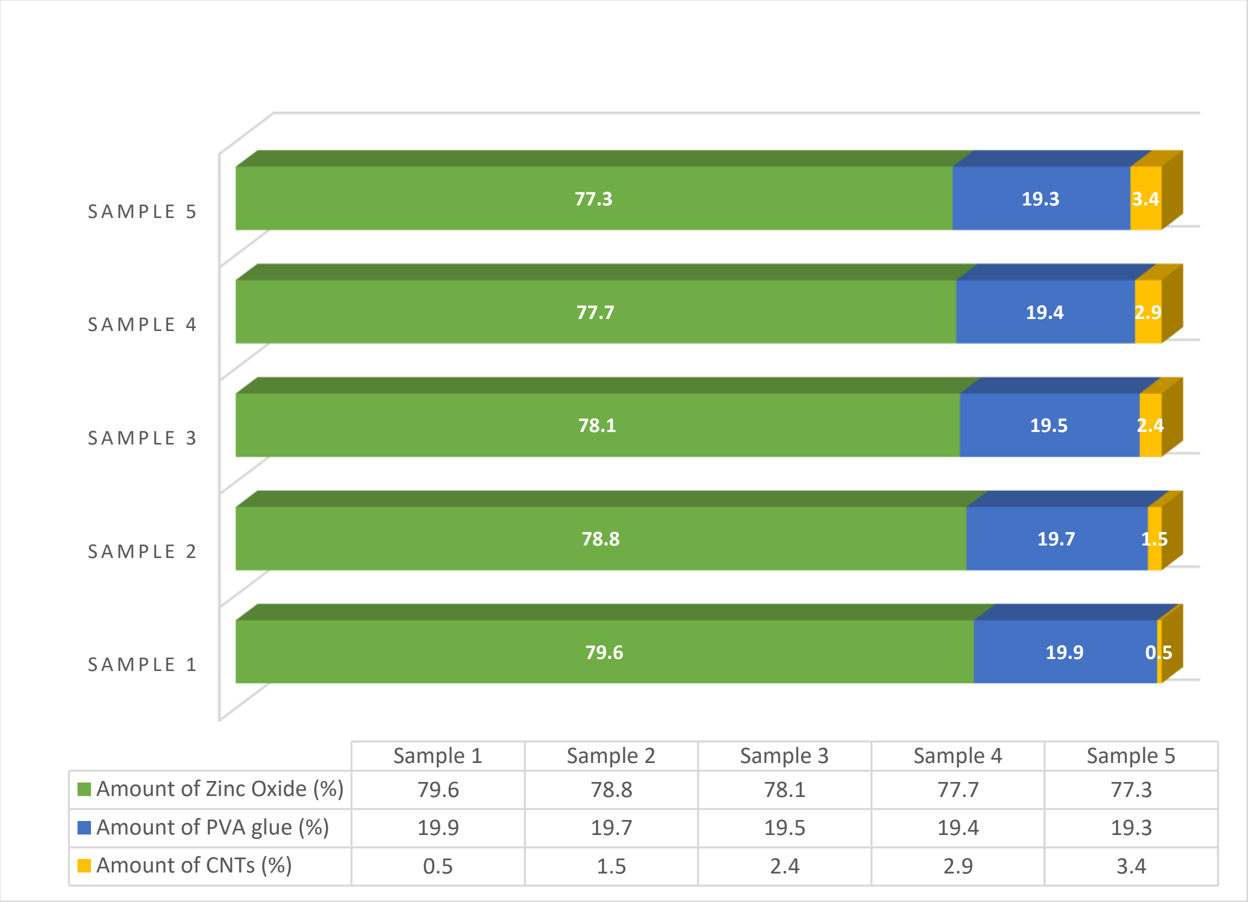

	Sample 1	Sample 2	Sample 3	Sample 4	Sample 5
🟩 Amount of Zinc Oxide (%)	79.6	78.8	78.1	77.7	77.3
🟦 Amount of PVA glue (%)	19.9	19.7	19.5	19.4	19.3
🟨 Amount of CNTs (%)	0.5	1.5	2.4	2.9	3.4

Figure 4-2: The varying composition (weight percentage in solution) of the main constituents of each paint.

Step 2: The resulting solution is applied to the metal surface (stainless steel) with the help of a syringe and a brush to reduce bubbles, which accentuates the formation of cracks. The solution on the surface of the metal plate dried out overnight in open air.

The paints bonded perfectly well to the surface and yielded tangible piezoelectric response. This method yields a paint that bonded to the metal surface. For the surface preparation, it was polished using an abrasive paper and washed but allowed to dry before the application of the paint. This method produced stronger and tougher paints after the usage of zinc oxide dispersion alone failed woefully. Figure 4.3 shows the painted steel surface. The sample 3 which contains 2.4 wt.% CNTs was used in Figure 4.3. In this work, a smooth stainless steel surface was used for the application of the paint. The painted steel surface was soaked in water for 24 hours and it remained intact but a pull-out test can be conducted to evaluate the experimental data for the bonding strength of the coating on a stainless-steel surface.

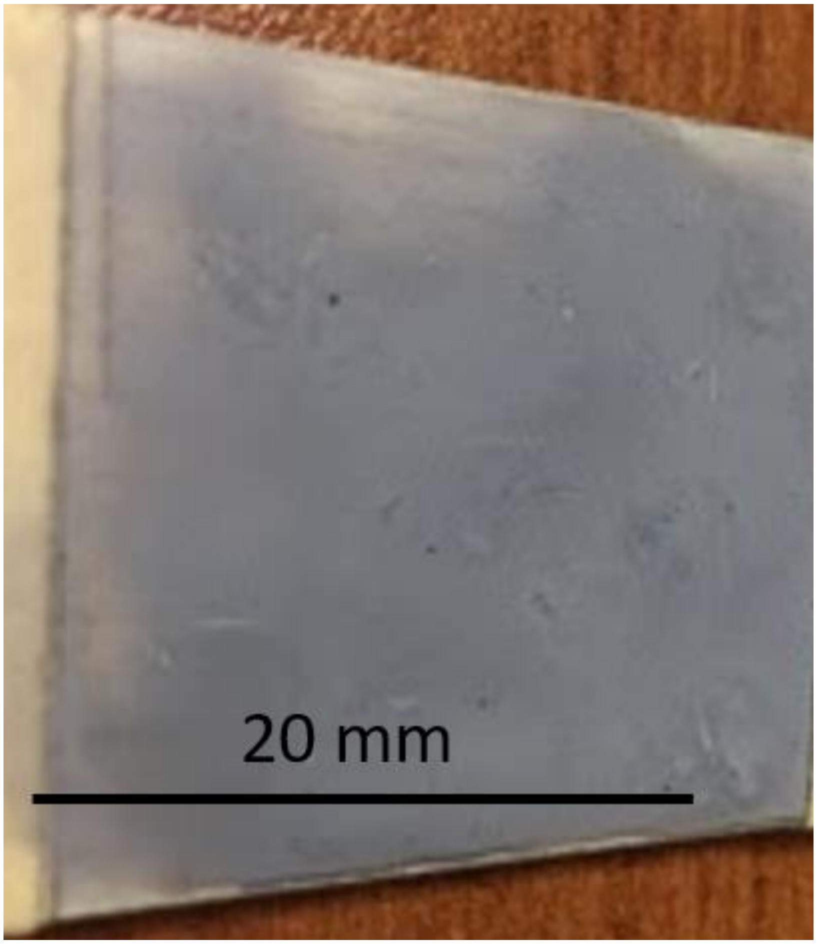

Figure 4-3: The nanocomposite solution containing 2.4wt.% CNTs yielded a smooth and strong paint when applied on a steel plate.

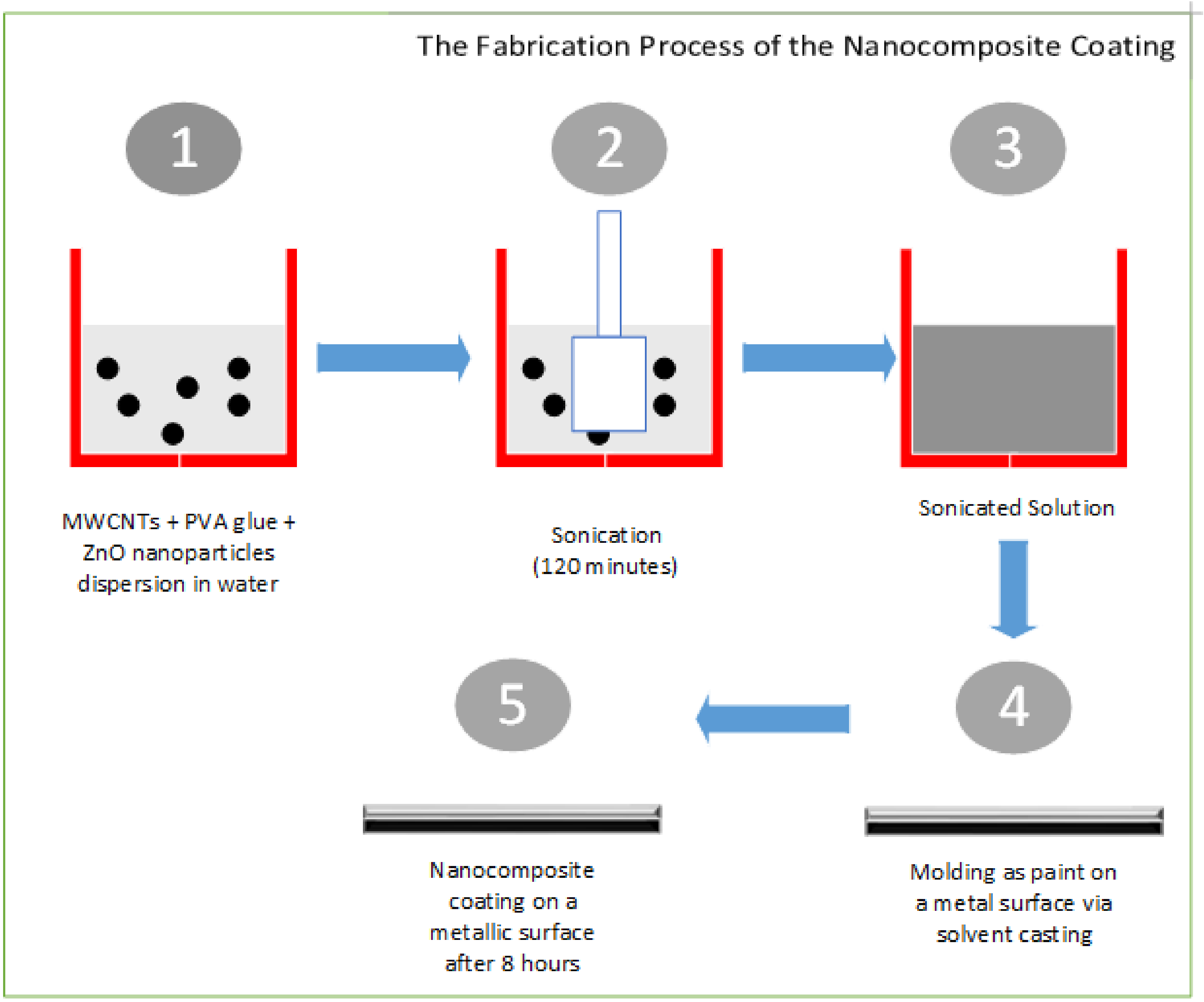

Figure 4-4: A schematic diagram showing the fabrication process of the nanocomposite paint.

Step 3: Addition of new layers to the metal surface as desired by repeating step 2. This is done and dried out before characterization because it leaves a thick layer (~130-150 µm) on the metal surface. For the paints used in this research, eight layers are made by repeating the process described in Figure 4.4.

4.3 Piezoelectricity Calibration

The LMS data acquisition system was used for the calibration of the piezoelectric coefficients of five paints made from the samples. The LMS system provides channels for measuring force via a force transducer input and other time-dependent quantities. The data acquisition system gives an accurate reading of these quantities at intervals of microseconds. The setup of the acquisition system is shown in Figure 4.5. The figure shows the LMS data acquisition system and the signal capture done during the test before the calculation of the piezoelectric coefficient along the poling direction of the nanocomposite paint.

An electrode is prepared and connected to one of the channels of the LMS system to monitor the voltage generated because of a static loading applied on the paint. The area of contact of the electrode with the surface of the paint is 0.6 cm X 0.7 cm. When a compressive force is applied to the paint via the electrode, the LMS system records both the force applied and the voltage generated by the piezoelectric composite paint. Each cycle of compressive loading is applied in a duration of 8 seconds.

For accurate readings, for each of the paints, the piezoelectric calibration is done at five different points and the average values of force applied and generated voltage are used for the piezoelectric calibration. The five different points are shown in Figure 4.6: at the four edges of the paint and the middle, all labeled 1 to 5.

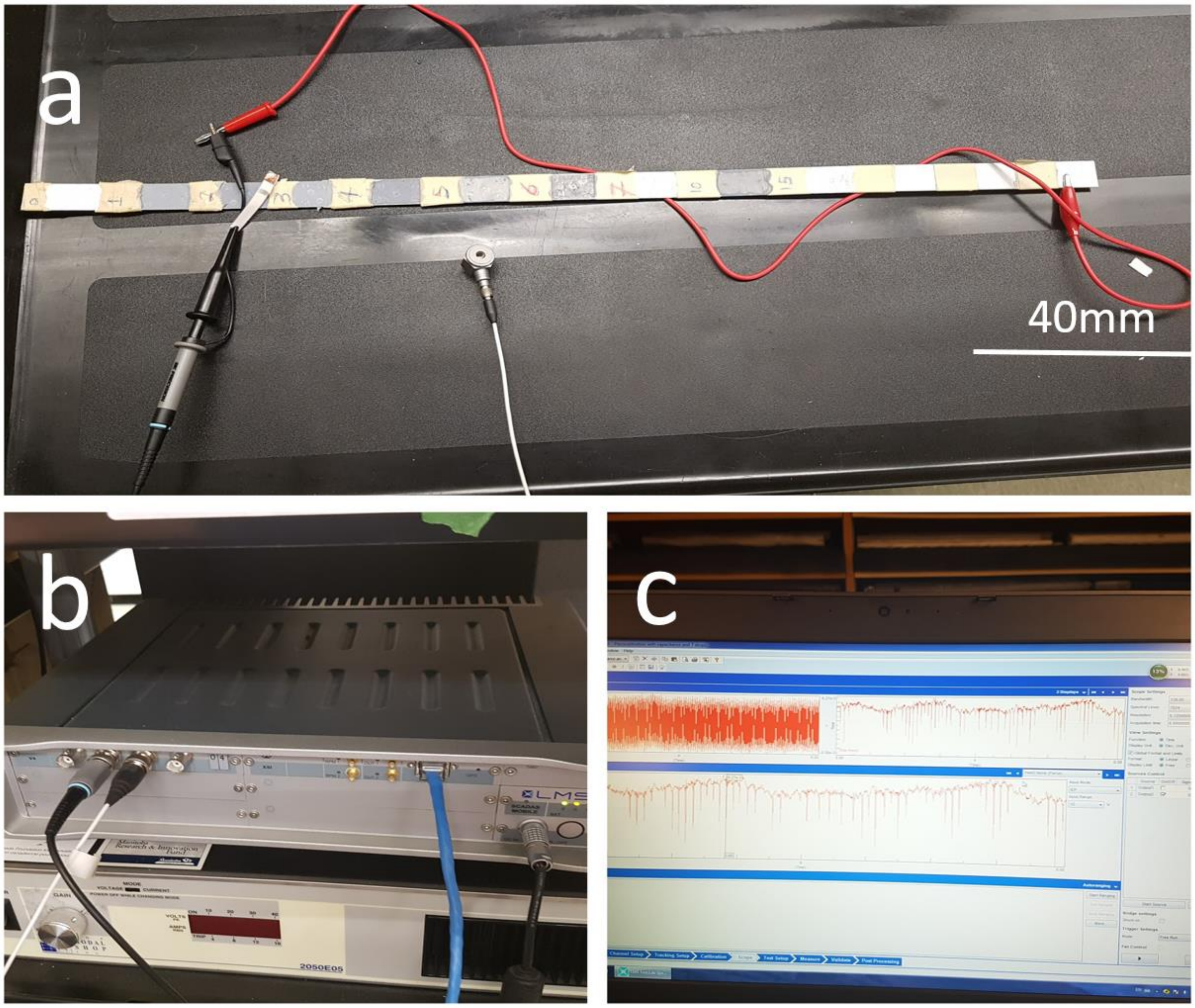

Figure 4-5: (a) The setup of the piezoelectric calibration showing the electrode, the force transducer, and the paints. (b) The back end of the LMS data acquisition system showing the two channels used for the readings of force applied and the voltage generated. (c) The front end showing the signal response of the readings from the electrode and force transducer during excitation of the paints.

The capacitances of the paints with the applied electrodes are obtained by a capacitance meter (High-Resolution Capacitance meter with PIC 16F628 by Roman Black®); it was specially designed to measure small capacitance even in the range of picofarads. The readings of the applied force and voltage output from one testing are plotted and shown in Figure 4.7 and Figure 4.8 respectively. From these graphs, the peak values of the voltage and corresponding maximum force applied on the paint are easy to find and used for calculating the piezoelectric coefficients.

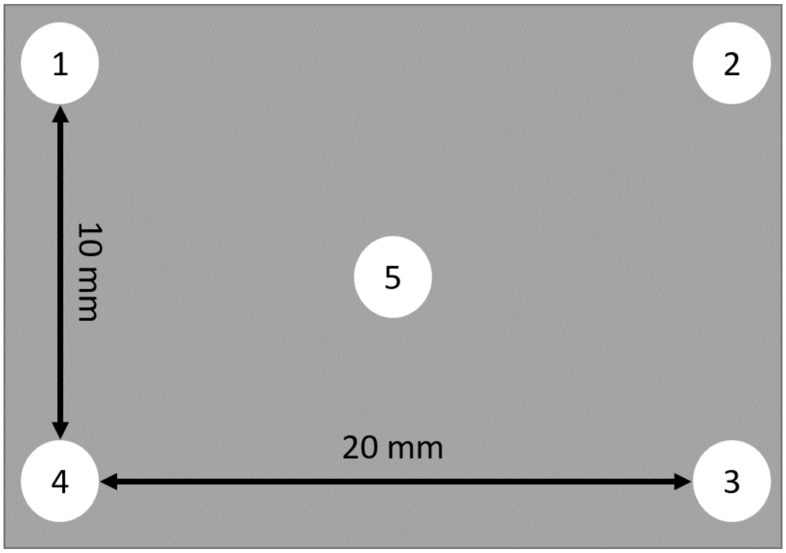

Figure 4-6: The simplified diagram showing the five different points of contact with the electrode and force transducer during the piezoelectric calibration.

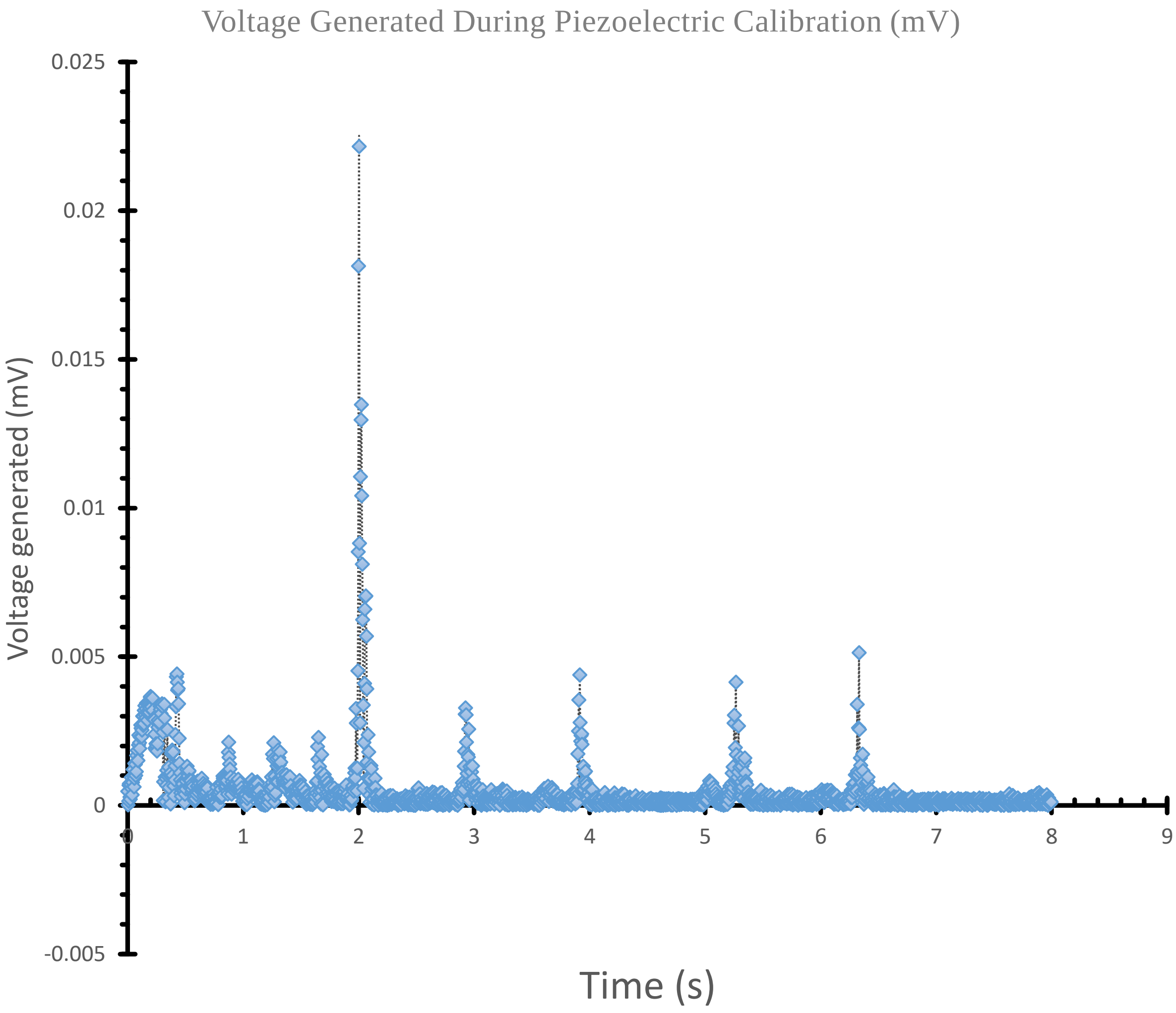

Figure 4-7: The plot of the voltage generated against time during the piezoelectric calibration of the paint.

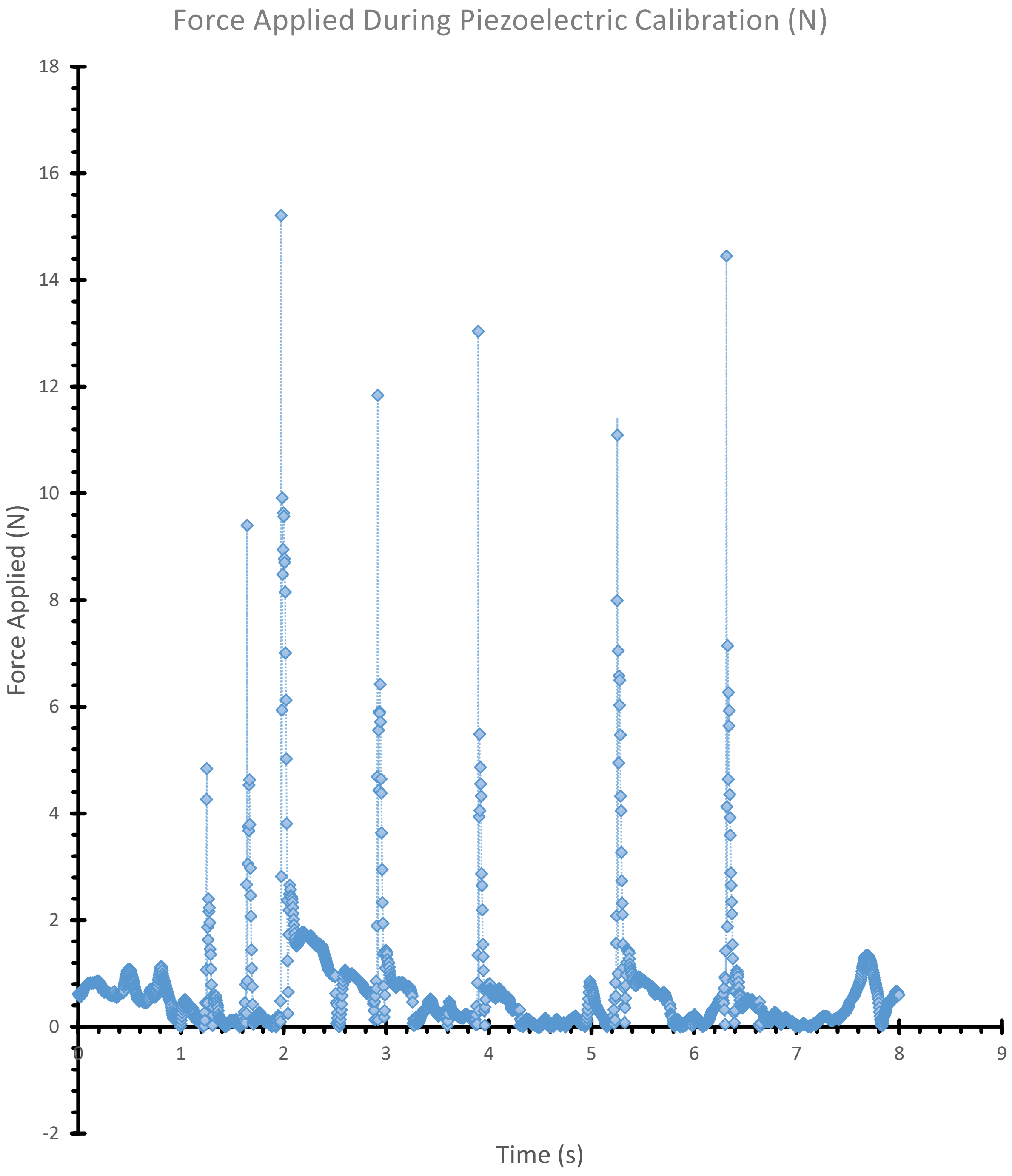

Figure 4-8: The plot of the force applied against time during the piezoelectric calibration of the paint.

Then, following simple calculations can be conducted to obtain a proper evaluation of the piezoelectric coefficient of the paints.

$$\mathbf{Q = C * V,} \qquad (4 - 1)$$

where Q is the total charge generated on the paint surface covered by the electrode, C is the capacitance of the paint at a specified point, and V is the voltage generated during excitation at a specified point.

$$\mathbf{D = Q/A_1,} \qquad (4 - 2)$$

where D is the charging density and A_1 is area of the electrode.

$$\mathbf{d_{33} = D/S,} \qquad (4 - 3)$$

where d_{33} is the piezoelectric coefficient and S is, the stress applied on the paint.

$$\mathbf{S = F/A_2,} \qquad (4 - 4)$$

where F is, the force applied on the paint and A_2 is an area of the tip of the force transducer.

After the calculation of each of these values for five different points on the paint, an average value is found to give an estimated value of the voltage generated and the average piezoelectric coefficient of each paint.

4.4 Microstructural Analysis

The Transmission Electron Microscope (TEM) was used because it produces images that are formed by interactions between the electrons and the sample. The sample can be analyzed for information concerning morphology, crystallography, and composition, with a possible spatial resolution of 0.1nm. The geometric dimensions of the major components of the nanocomposite paint; zinc oxide nanoparticles dispersion and carbon nanotubes are in the range of nanometers (nm).

In this research work, the dip coating approach in the nanocomposite solution was used while preparing samples to be viewed under TEM for the microstructural characterization of the solution that was used for the paint. The FEI Talos® Field Emission Scanning Transmission Electron Microscope operating at 200KV equipped with High-Angle Annular Dark-Field (HAADF) detector and Super-X EDS detector for compositional analysis was used for the microstructural study.

However, for the microstructural investigation of the dried-out nanocomposite paints for the presence of voids, the Scanning Electron Microscopy (SEM) was employed. The SEM images were taken using the FEI Nova Nano 450 SEM which is a Field Emission nano SEM equipped with Energy-Dispersive Spectroscopy (EDS), Wavelength-Dispersive Spectroscopy (WDS) and Electron Backscatter Diffraction (EBSD) detectors.

4.5 Nano-indentation Test

To test the mechanical properties of the nano piezoelectric paints, the most efficient technique is to use nano-indentation. For the nano-indentation tests, samples are prepared by mounting steel strips on Bakelite using the mounting press. The solvent casting method is used for applying several layers of paints on a metal surface. It takes about eight hours for each layer to dry out and give a solid paint, this is repeated eight times to get a paint (~130-150 µm in thickness), which is thick enough for nano-indentation without reaching to the sub-metal surface during the testing. This was done for the five different types of paints with varying proportions of CNTs.

After drying out, grinding is done for 30 minutes on each of the samples using the Silicon Carbide (SiC) abrasive paper with 1200 grit size under a water cooling system. Making the surface of the paint flat and smooth for nano-indentation. The polishing takes place with a fine cloth and 1-micrometer alumina solution for five minutes after washing the surface with clean warm water. The sample was dropped inside a beaker filled with ethanol and placed in an ultrasonic bath for another five minutes. The comprehensive cleansing is necessary to make the surface of the paints void of any unwanted particles.

Hysitron triboindentor TI-950 with standard Berkovich tip is used for the nano-indentation tests. The maximum load is kept at 150 μN. Before performing the test, the machine is calibrated and the area function is calculated using known fused Quartz sample. The load function is the standard trapezoid, which consists of loading rate of 30 μN/s and holding for 2 s and unloading with same loading rate.

For each indentation process, there are three key steps as shown in Figure 4.9: loading from point A to point B, holding at maximum load (150 μN) for 2 s from B to C and unloading occurs from point C to point D. Finally, the samples are fully unloaded.

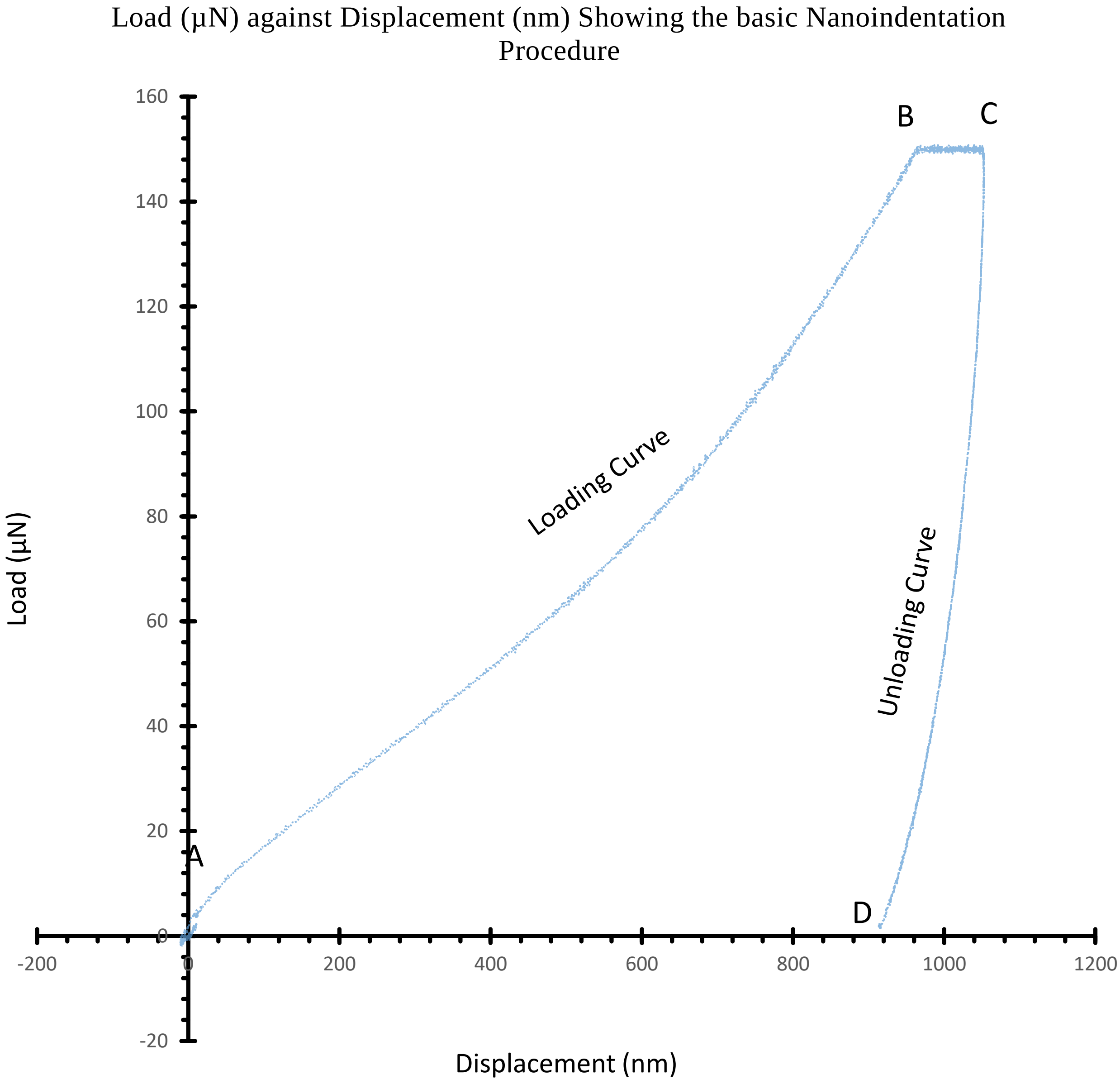

Figure 4-9: The Nano-indentation basic procedure showing the loading, holding and unloading processes as reflected on the Load-displacement curves.

The acquired data from the nano-indentation tests are in the form of load-displacement curves and the standard Oliver-Pharr method [83] is used for extracting the values of Nano-indentation hardness (H_{it}) and Young's modulus. The Nano-indentation hardness (H_{it}) is calculated by dividing the maximum force by the projected surface area and then converted to MPa as shown in equation 4-5,

$$\boldsymbol{H_{it} = \frac{P}{A_p}}, \tag{4 - 5}$$

where A_p is the projected surface area under the maximum load (P). The calculations were automatically generated by the nano-indentation machine based on these equations.

The reduced modulus E* was evaluated using one of the equations from the Oliver-Pharr method as shown in equation 4-6,

$$\boldsymbol{E^* = \frac{1}{2}\sqrt{\frac{P}{A_p}\frac{dp}{dh}}}, \tag{4 - 6}$$

The modulus of elasticity E was determined using equation 27,

$$\boldsymbol{\frac{1}{E^*} = \frac{1-\nu^2}{E} + \frac{1-\nu_i^2}{E_i}}, \tag{4 - 7}$$

where the modulus of elasticity and the Poisson ratio of the indenter are E_i and ν_i respectively.

The nano-indentation is carried out with 12 different indentations on each paint giving 12 readings and the mean values are used in calculating the Young's Modulus and Hardness of each paint.

Chapter 5 Results and Discussion

In this section, the results of the microstructural analysis, the piezoelectric calibration and mechanical characterization of the fabricated paint are presented and discussed.

5.1 Microstructural Analysis

The zinc oxide nanoparticles in the composite contribute mainly to the piezoelectric property of the paint. When the nanocomposite solution with 2.4 wt.% of CNTs was examined by the Transmission Emission Microscope (TEM) as shown in Figure 5.1; it shows zinc oxide nanoparticles dispersed within the matrix. The images reveal the connection between the ZnO particles and CNTs; the CNTs increase the proximity between the ZnO particles and serve as electrical bridges which consequently increases the number of possible paths of electrical conduction between ZnO particles in the paint.

The enhanced electrical connectivity of the ZnO particles in the composite because of the addition of CNTs will help to connect and accumulate the electric field generated by ZnO particles which positively affects the piezoelectric response of the paints. Figure 5.2 shows the Energy Dispersive Spectrometry (EDS) graph which confirmed the chemical composition of the micrograph in Figure 5.1. EDS is an analytical technique which was used for the chemical characterization of the nanocomposite solution, and from Figure 5.2 it can be deduced that the solution contains carbon, oxygen, zinc, and copper. The copper is not part of the solution but from the copper grid mesh used for the TEM sample preparation.

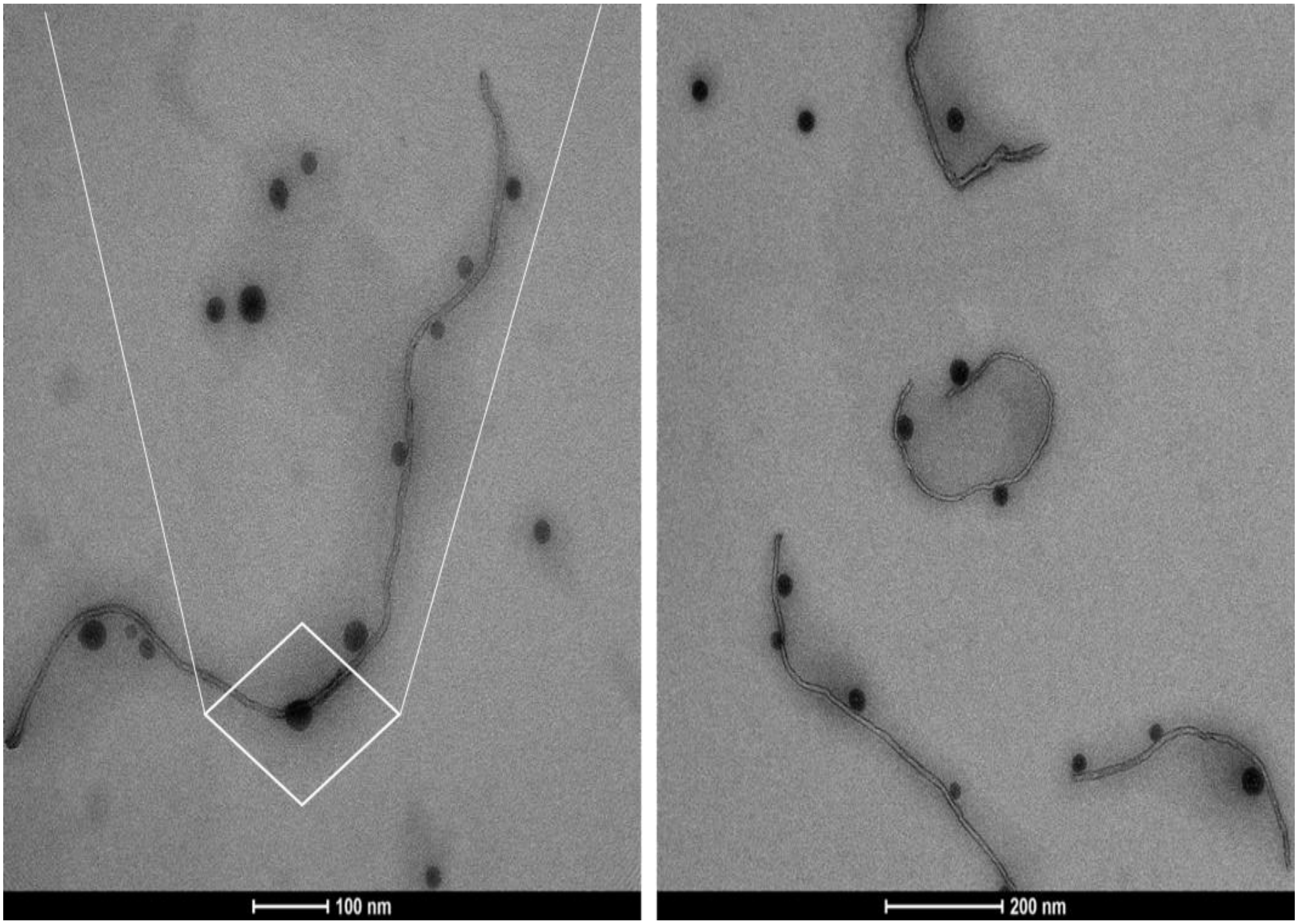

Figure 5-1: The TEM images of the nanocomposite solution (2.4wt.%) showing the CNTs connecting the zinc oxide nanoparticles and the rectangle shows the spot used for the Energy Dispersive Spectrometry (EDS).

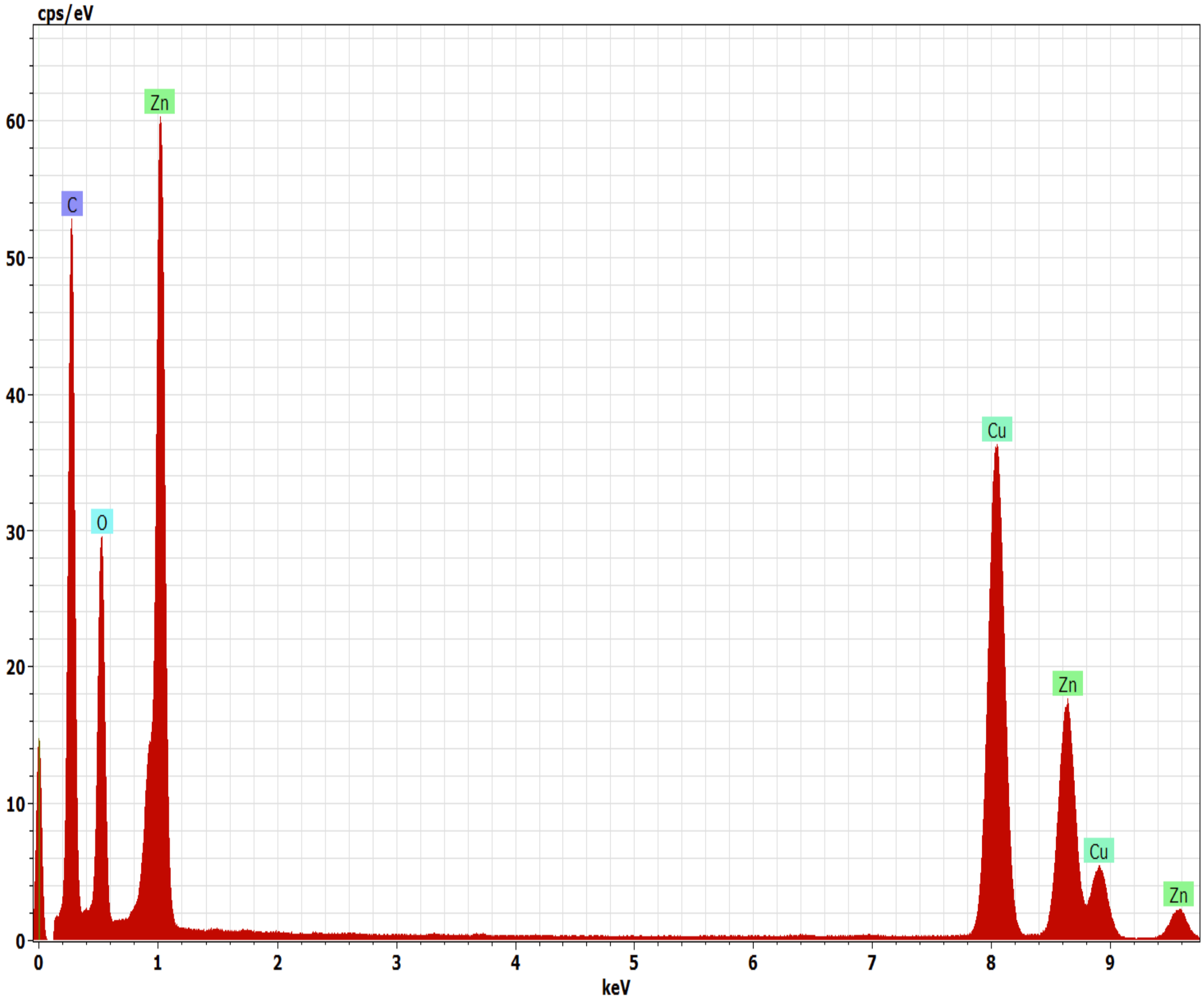

Figure 5-2: The Energy Dispersive Spectrometry (EDS) graph with TEM showing the major components of the nanocomposite solution (2.4 wt.% CNTs).

5.2 Piezoelectric Calibration

From the LMS data acquisition system used for the piezoelectric calibration of the paints, data acquired are used for the determination of the piezoelectric coefficients of the paints. The piezoelectric coefficients are calculated based on equations (4-1) – (4-4). The mean and maximum values of the piezoelectric coefficients of the paints are presented in Table 5.1.

Table 5-1: The maximum and average piezoelectric coefficients of the different nano-composite paints after the piezoelectric calibration.

Types of Paint	**Maximum Piezoelectric Coefficient (pC/N)**	**Mean Piezoelectric Coefficient (pC/N)**
With 0.5% CNTs	0.094	0.068±0.02
With 1.5% CNTs	0.278	0.184±0.08
With 2.4% CNTs	0.812	0.405±0.27
With 2.9% CNTs	0.535	0.238±0.18
With 3.4% CNTs	0.039	0.024±0.01

In the calibration of the nanocomposite paint, the lack of homogeneity in the paint posed a serious challenge to the proper evaluation of the piezoelectric coefficients. In a bid to reduce the effect of the non-homogeneity, five different points are chosen on each paint for the piezoelectric calibration as shown in Figure 4.6.

Figure 5.3 shows the effect of increment in the weight percentage of CNTs in the nanocomposite paint on their piezoelectric responses with respect to their maximum piezoelectric coefficients. Figure 5.3 shows that an increase in the amount of CNTs improves the piezoelectric coefficients of the paints until there is a sharp decline at a threshold value. In Figure 5.3, the highest piezoelectric coefficient of 0.812 pC/N is recorded when the weight percentage of CNTs in the paint is at 2.4%. The maximum values of the piezoelectric coefficients drop gradually with increments in the weight percentage of the CNTs in the paint. The piezoelectric coefficient dropped from the threshold value (0.812pC/N) by over 1000% to 0.039 pC/N when the weight percentage of the CNTs in the paint is at 3.4%. This behavior shows that excess CNTs in the paint has detrimental effects on the effectiveness of the paint piezoelectricity.

In Figure 5.4, the mean values of the piezoelectric coefficient of the paint are plotted against the varying weight percentages of CNTs in the paint. The graph shows a consistent behavior with Figure 5.3 which implies that evaluation of the average value of the piezoelectric coefficients from five different points on each paint compensated for any form of inhomogeneity that may be inherent in the paint. The threshold value of the mean piezoelectric coefficients is 0.405 pC/N which occurred at 2.4 wt.% of CNTs in the paint.

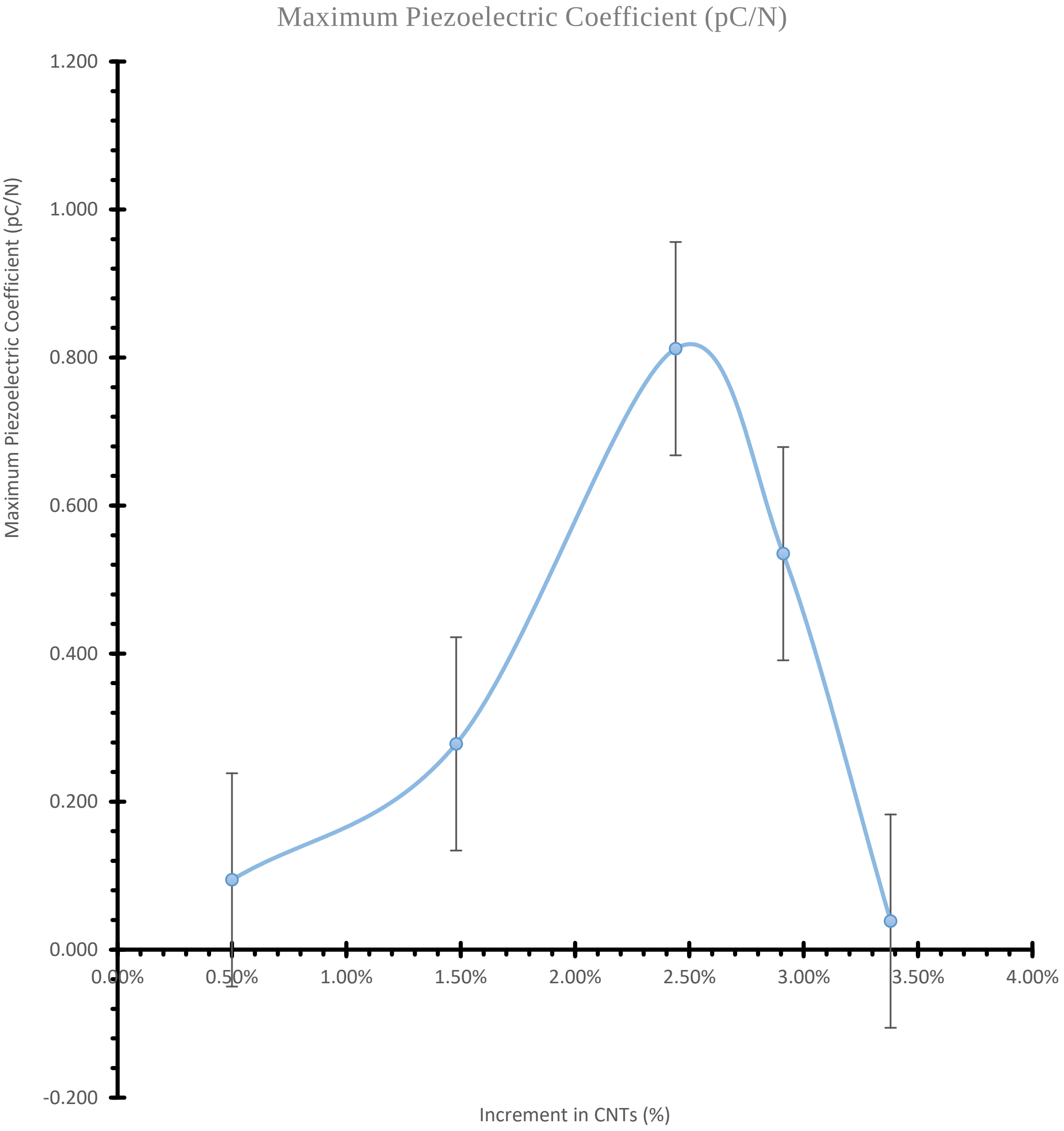

Figure 5-3: The effect of an increment in CNTs on the maximum piezoelectric coefficients of the nanocomposite paint.

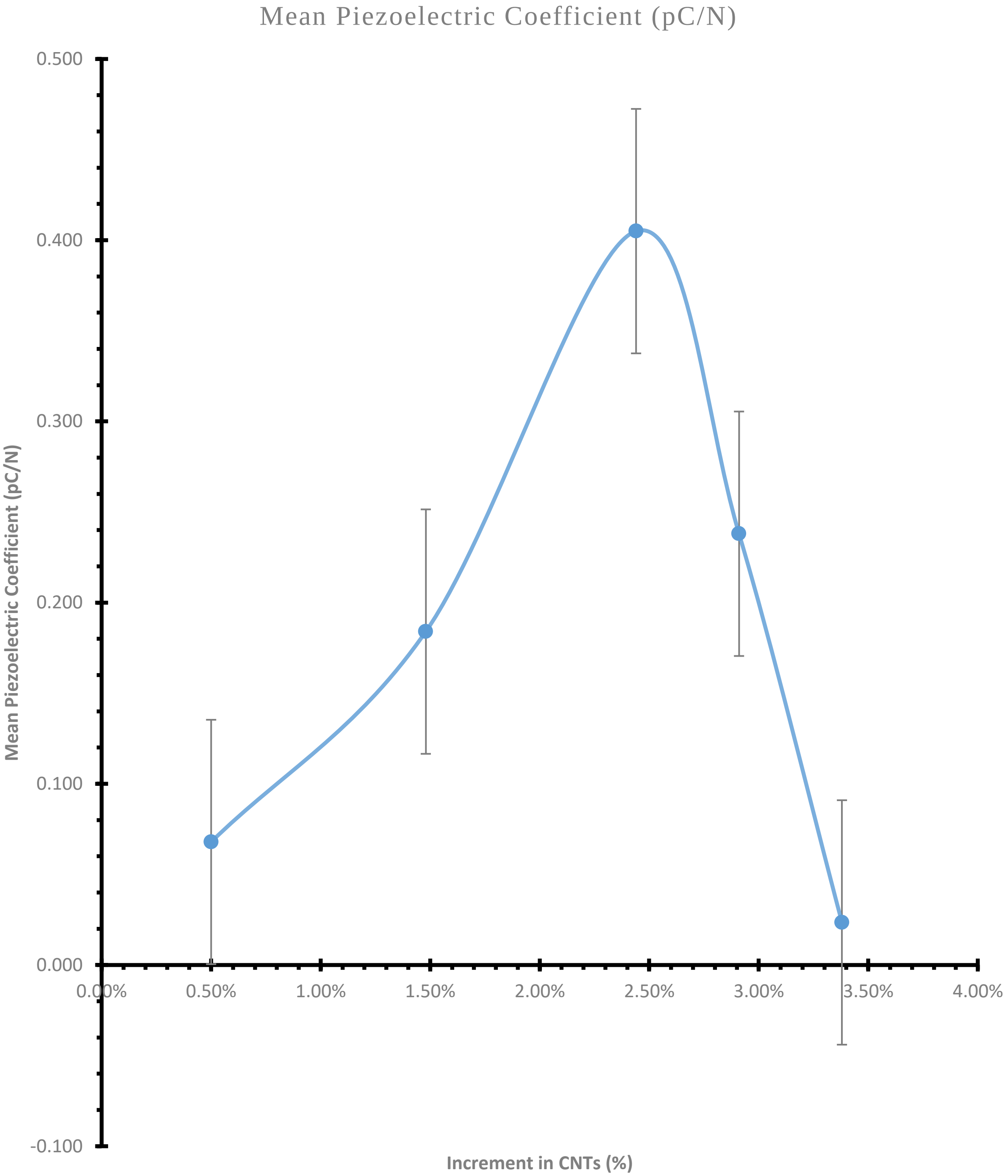

Figure 5-4: The effect of an increment in CNTs on the mean piezoelectric coefficient of the nanocomposite paint.

As seen in Figures 5.3 and 5.4, the results of the piezoelectric calibration indicate a switch in the piezoelectric response of the paints with respect to increase in the amount of CNTs added. While focusing on the positive side of the results, the increment in the addition of the CNTs to the paints improved its piezoelectricity and this can be attributed to the enhanced electrical connectivity and bridging of different ZnO nanoparticles as observed in the TEM micrograph.

In addition, a similar behaviour is observed in energy storage-related work [84], [85][86], researchers have proposed CNTs as conductive additives to the positive electrodes of lithium-ion batteries because it yields stronger electrical connectivity in the active materials of the battery cells thereby increasing the lifecycle of the battery. It was concluded that the increased electrical connectivity in the batteries stems from the uniformly distributed CNTs which increases the number of possible paths of electrical conduction[85] to bridge nano particles.

However, more CNTs dispersion (>2.4% weight percent) in the paint will lead to excess voids in the paint and gaps after its drying out which affects electrical connection between ZnO particles. In this case, electrical potential generated by many isolated ZnO particles subjected to external loading cannot be connected leading to the lower final voltage output from the composite paint and smaller piezoelectric coefficient. The sharp decline in the piezoelectric coefficients of the paints at a specific threshold can hence be dignified with the discussions above.

5.3 Nano-indentation Test

The results of the nano-indentation of the piezoelectric nano-composite paint with different weight percentages of CNTs are presented in Table 5.2 alongside the plotted graphs in Figures 5.5 and 5.6. Table 5.2 shows the mean values of the Hardness and Young’s modulus of the different samples tested with their error bars. The Young’s modulus (in Figure 5.5) and the hardness of the nanocomposite paints (in Figure 5.6) increase to 1080MPa and 17MPa with the addition of more

CNTs until it reaches 2.4% of weight percentage but begins to decrease with more CNTs with 2.9% and 3.4% of weight percentage.

Table 5-2 – The mean values of Young's modulus and hardness of the different nano-composite paints with error bars.

Types of Paint	**Mean Young's modulus (MPa)**	**Mean Hardness (MPa)**
With 0.5% CNTs	352.53 ± 91.14	7.32 ± 2.46
With 1.5% CNTs	500.78 ± 146.35	10.36 ± 3.34
With 2.4% CNTs	1032.70 ± 207.60	16.90 ± 4.15
With 2.9% CNTs	920.33 ± 272.77	15.11 ± 6.49
With 3.4% CNTs	525.34 ± 170.04	13.59 ± 3.83

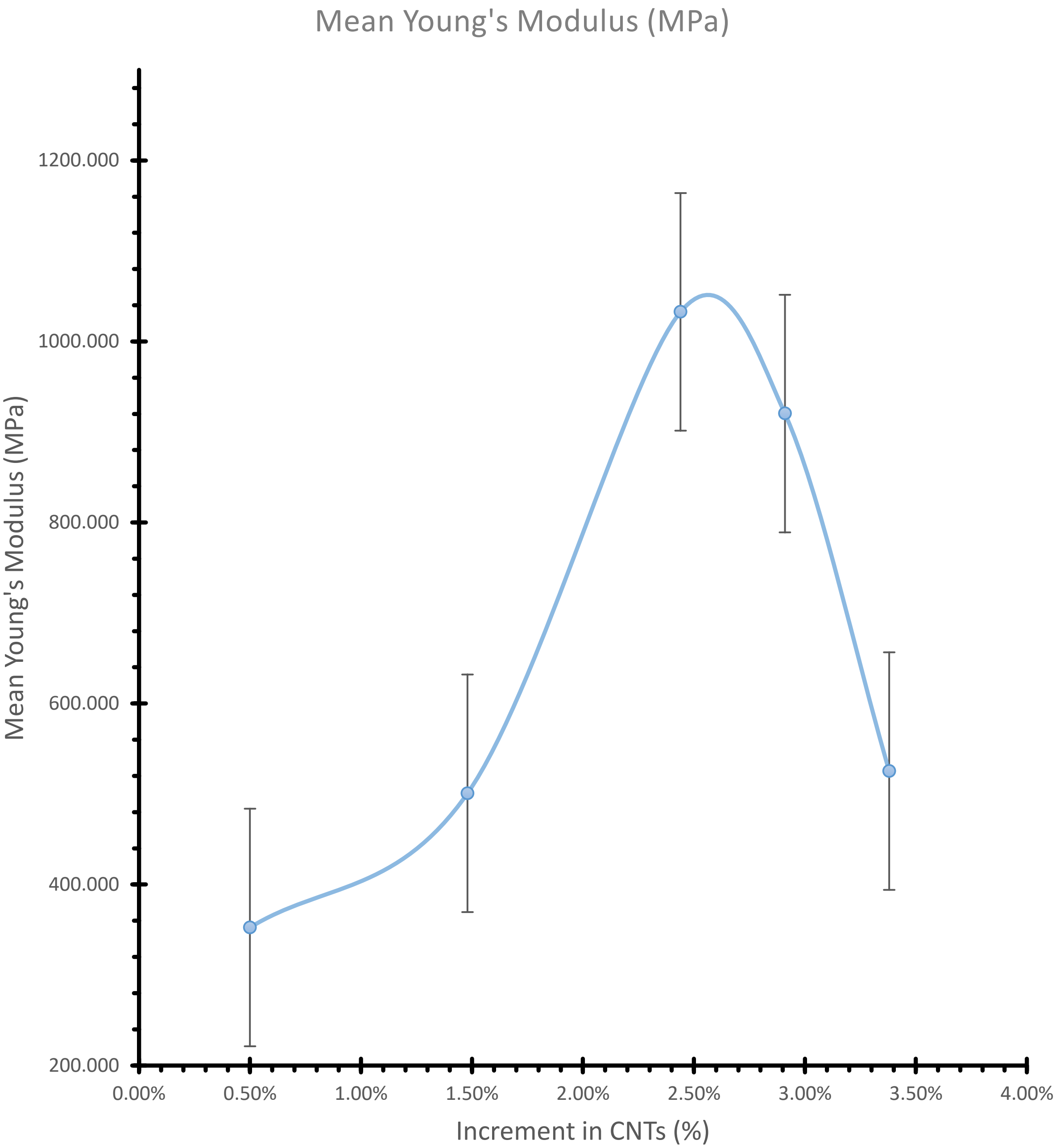

Figure 5-5: The effect of increment in CNTs on the Young's Modulus of the nanocomposite paint.

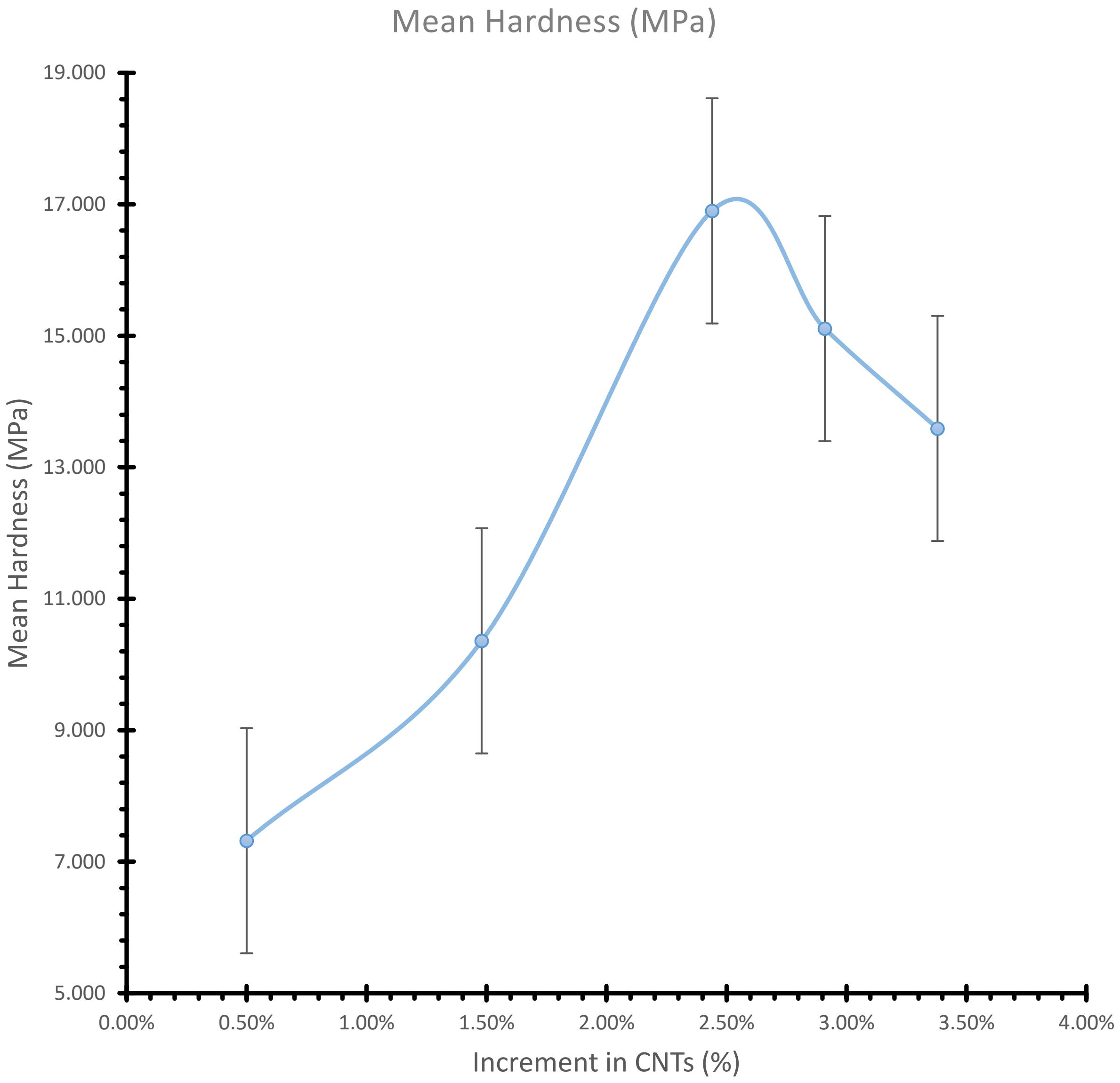

Figure 5-6: The effect of increment in CNTs on the hardness of the nanocomposite paint.

The results of the nano-indentation tests for the various types of paints show that there is an improvement in the mechanical properties of the paints with an increase in the addition of CNTs. Asides serving as electrical bridges to join various zinc oxide nanoparticles in the dispersion, it reinforces the Young's Modulus of the nano-composite paint and its hardness. The increment may be related to the exceptional mechanical properties of CNTs since they are known to have high Young's modulus and hardness [72] [73].

Although the mechanical characterization of the nanocomposite paints displays an appreciable influence of CNTs on the mechanical properties of the paints, the CNTs also play the role of enhancing the piezoelectric and electrical properties of the zinc oxide by creating electrical bridges among the nanoparticles. To validate the presence of the CNTs and their roles as linkages for the zinc oxide nanoparticles, the micrographs and EDS scan of the nanocomposite solution (Figures 5.1 and 5.2) as seen via the TEM provide useful information.

However, it should be noted that when CNTs added to the paint reaches a threshold, the mechanical properties of the paints begin to diminish and characterized by low Young's Modulus and hardness values. The downward slide in the quality of mechanical properties of paints can be attributed to the accumulation of residual moisture in the layered paints with an increase in CNTs dispersion. The residual moisture creates discontinuities in the microstructure of the nanocomposite paint which is visible in form of voids as shown in Figure 5.7. Figure 5.7 is the SEM image of a dried-out coating produced from the nanocomposite paint containing 3.4 wt.% CNTs while Figure 5.8 shows the SEM image of sample 3 which contains 2.4 wt.% CNTs. The preponderance of voids in Figure 5.7, when compared to Figure 5.8, confirms the effect of excess CNTs on the hardness and Young's modulus of the nanocomposite paints. The increase in the amount of CNTs water dispersion added to the nanocomposite solution increases the probability of having residual moisture in the layers of coatings leading to more voids in the dried-out paint.

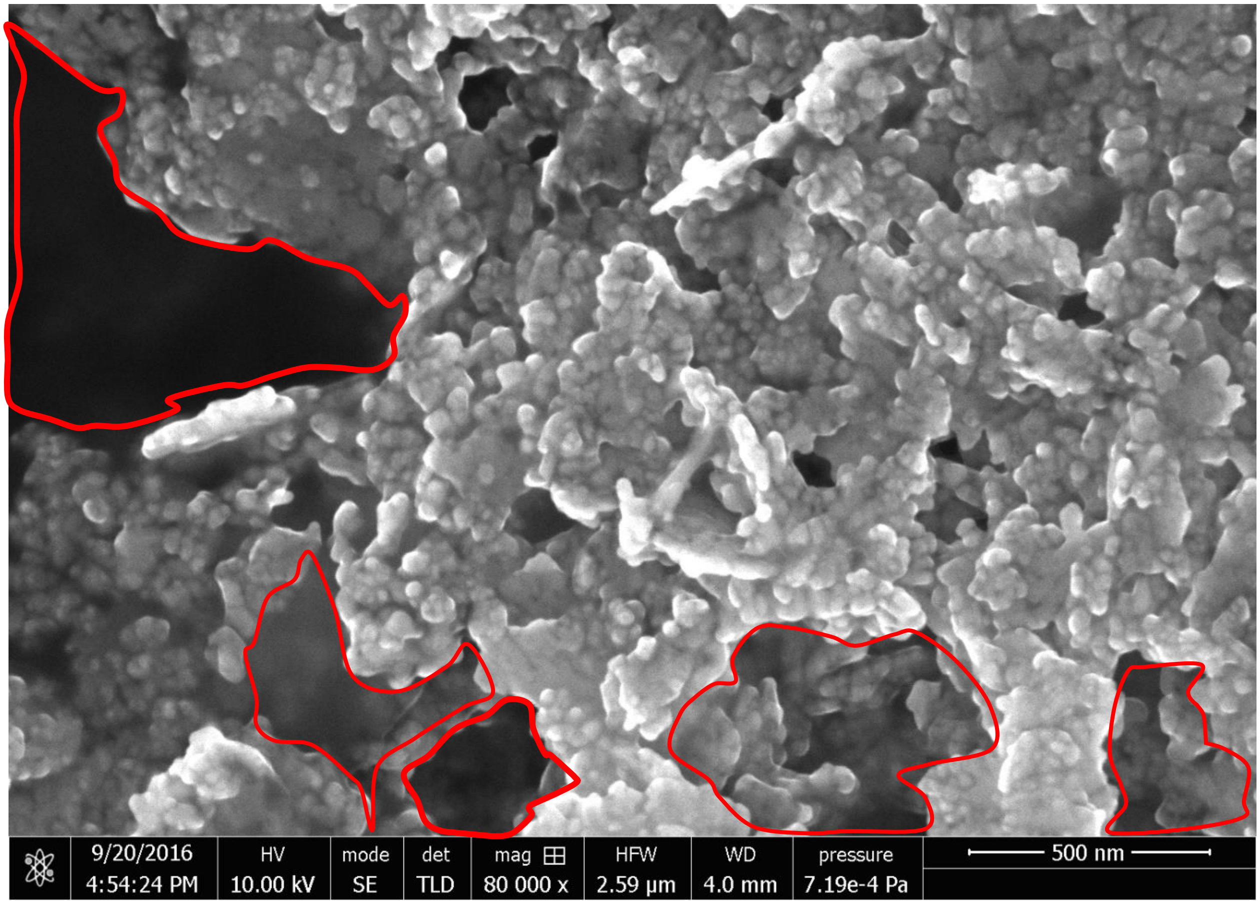

Figure 5-7: The SEM image of the nanocomposite paint containing 3.4 wt.% CNTs showing voids in the microstructural level, the red rings depict voids.

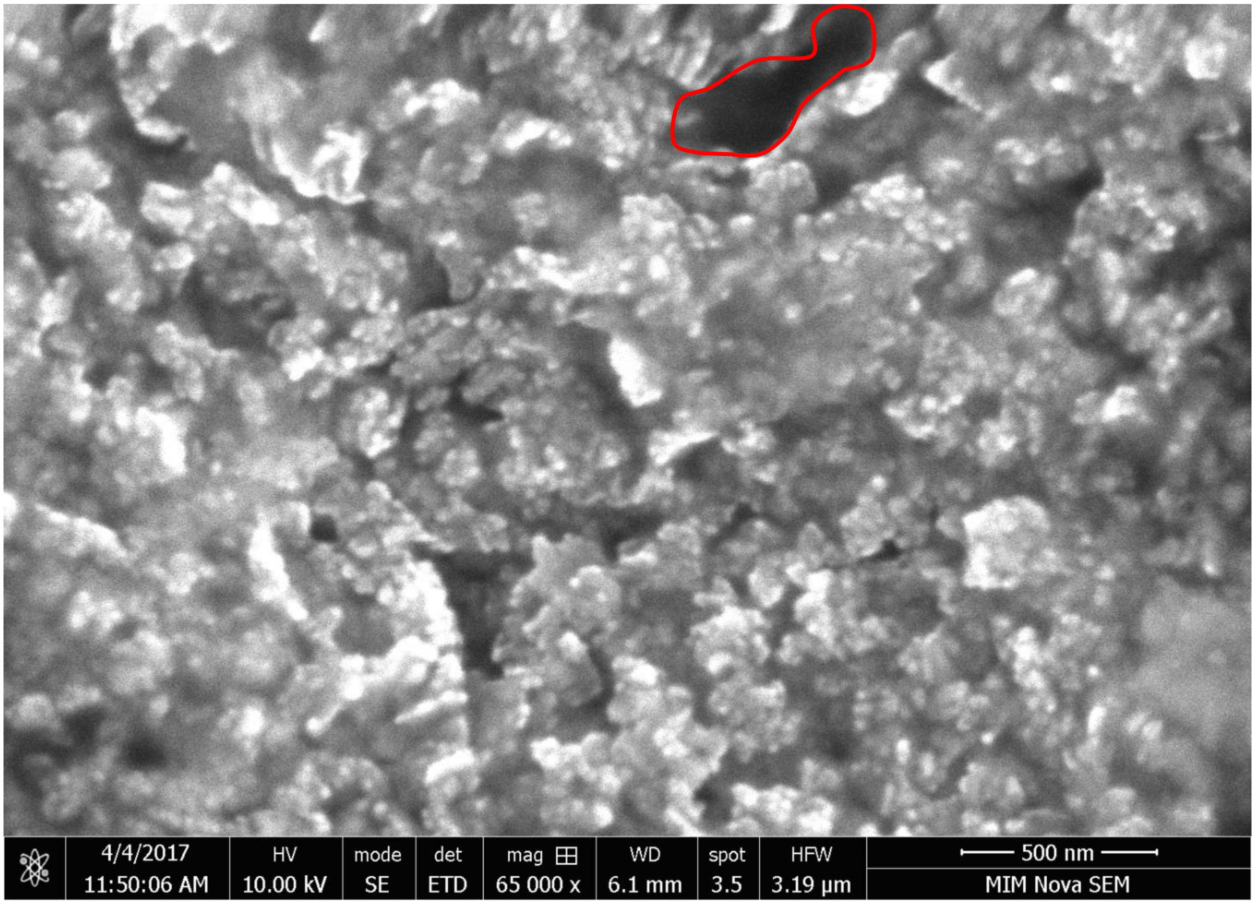

Figure 5-8: The SEM image of the nanocomposite paint containing 2.4 wt.% CNTs showing voids in the microstructural level, the red ring depicts a void.

Furthermore, Sun et al. [87] investigated the effects of local void defects on the mechanical properties of silicon and diamond films using the nano-indentation process, they also found out that Young's modulus and hardness of the films reduce significantly due to the existence and proliferation of local void defects.

The solvent used as the dispersal medium of the materials in the composite may remain as residue in the composites and affect both electrical conductivity and mechanical property of the material. Bryning et al. [88] reported that residual solvent in SWCNT-based epoxy nanocomposites adversely affects the transport and mechanical properties of the cured composites because it is capable of inhibiting the nucleophile-electrophile interactions between the epoxy and the hardener. Coupled with these manifestations of intrinsic mechanical deformities, it has a physical appearance of a paint laden with pores and cracks, when excess CNT solution is added.

The switching behavior seen in the mechanical properties of the composite coatings was observed in a similar work; Koumoulos et al. [89] performed the evaluation of surface properties of a polymeric composite: epoxy matrix composite reinforced with nano-diamond (ND) particles. It was reported that at a concentration threshold of 2 wt.% NDs in the composites, the mechanical properties exhibited a switching behavior characterized with low Hardness and Young's Modulus values.

In summary, the increment in the CNTs added to the nanocomposite paint has a positive effect on its core mechanical properties (Young's Modulus and Hardness) and piezoelectric coefficient, but when it is in excess, the excellent mechanical properties and piezoelectric coefficients are negatively impacted. The optimized amount of CNTs as observed from experiments stands at 2.4 wt.% CNTs addition to the nano-composite paint for desired enhanced mechanical and piezoelectric properties.

Chapter 6 Conclusions and Future Work

In this thesis, robust attention is given to the design, production, and analysis of a piezoelectric nanocomposite paint that can be used for damage detection in structures. It started with the provision of a solid background knowledge of how damage in structures is handled via SHM. It highlighted the major SHM methods deployed by engineers in the early detection and location of damage in structures. The review of several methods involving the use of sensors made from piezoelectric materials while taking into consideration the use of CNTs in enhancing the effectiveness of the sensors followed. Numerical modeling using MATLAB showing a simulation of a delaminated cantilever beam with its top surface covered with a piezoelectric coating is proposed as a method of verifying the feasibility of a piezoelectric paint capable of multipoint strain sensing in SHM applications.

This research work validates the possibility of producing a piezoelectric nanocomposite paint made of zinc oxide (ZnO), Poly Vinyl Alcohol (PVA) glue and Carbon Nanotubes (CNTs) using the solvent casting method. It further reinforces the standing notion that the piezoelectricity effect of composites made from zinc oxide can be enhanced by the addition of CNTs which serve as electrical bridges to link the piezoelectric nanoparticles to one another. It also shows that there is a threshold amount in weight percentages of CNTs that can be added to a nanocomposite for the best performance in terms of piezoelectric output and mechanical strength. The concentration threshold of the addition of CNTs is seen in Sample 3 as shown in Figure 4.2: 78.1% ZnO, 19.5% PVA glue and 2.4% CNTs.

Overall, the uniqueness of the research work is the development of a piezoelectric paint that can be easily applied as a paint/thin coating on metallic surfaces and bonds perfectly well with enhanced piezoelectricity and mechanical properties. The newly developed nanocomposite smart paint material has potential applications in the field of strain sensing and piezoelectric transducers.

However, the research work is in its introductory stage and exhibits significant potential for notable applications in SHM. Future research work should include a series of experiments to test the piezoelectric response of the paints under dynamic loadings. Further studies are required to carry out the on-field testing of the paint as a damage detection sensor. Lastly, other methods of paint solution preparation and fabrication such as melt-mixing, extrusion, and 3D printing should be explored to reduce the voids in the paint after drying out.

References

[1] S. W. Doebling and C. R. Farrar, “Structural Health Monitoring: An overview of an evolving research area,” *Struct. Heal. Monit.*, vol. 2, 1996.

[2] A. G. A. Rahman, Z. Ismail, S. Noroozi, and O. Z. Chao, “Study of open crack in rotor shaft using changes in frequency response function phase,” *Int. J. Damage Mech.*, vol. 22, no. 6, pp. 791–807, 2013.

[3] M. B. Duggan and O.O. Ochoa, “Natural Frequency Behavior of Damaged Composite Materials,” *J. Sound Vib.*, vol. 158, no. 3, pp. 545–551, 1992.

[4] D. Barazanchy, M. Martinez, B. Rocha, and M. Yanishevsky, “A hybrid structural health monitoring system for the detection and localization of damage in composite structures,” *J. Sensors*, vol. 2014, 2014.

[5] K. S. C. Kuang, “Distributed damage detection of offshore steel structures using plastic optical fibre sensors,” *Sensors Actuators A Phys.*, vol. 229, pp. 59–67, 2015.

[6] G. J. Sylvester, “Electronic Theses and Dissertations Damage Detection in Plate Structures using Guided Ultrasonic Waves,” 2013.

[7] A. S. Islam and K. C. Craig, “Damage detection in composite structures using piezoelectric materials,” vol. 318, 1994.

[8] P. P. Kumar, B. V. Soma Sekhar, K. Balasubramaniam, C. V. Krishnamurthy, and B. Maxfield, “In-situ damage detection in plate structures using PWAS and non-contact Laser Doppler Velocimeter,” *AIP Conf. Proc.*, vol. 894, pp. 1509–1515, 2007.

[9] S. A. M. Al-Said and A. A. Al-Qaisia, “Influence of crack depth and attached masses on

beam natural frequencies," *Int. J. Model. Simul.*, vol. 28, no. 3, pp. 239–247, 2008.

[10] F. N. Meyers, K. J. Loh, J. S. Dodds, and A. Baltazar, "Active sensing and damage detection using piezoelectric zinc oxide-based nanocomposites.," *Nanotechnology*, vol. 24, no. 18, p. 185501, 2013.

[11] K. J. Loh and D. Chang, "Zinc oxide nanoparticle-polymeric thin films for dynamic strain sensing," *J. Mater. Sci.*, vol. 46, no. 1, pp. 228–237, 2011.

[12] H. Gullapalli *et al.*, "Flexible piezoelectric zno-paper nanocomposite strain sensor," *Small*, vol. 6, no. 15, pp. 1641–1646, 2010.

[13] N. R. Alluri, B. Saravanakumar, and S.-J. Kim, "Flexible, Hybrid Piezoelectric Film ($\mathrm{BaTi}_{(1-x)}\mathrm{Zr}_{x}\mathrm{O}_{3}$)/PVDF Nanogenerator as a Self-Powered Fluid Velocity Sensor," *ACS Appl. Mater. Interfaces*, vol. 7, no. 18, pp. 9831–9840, May 2015.

[14] S. Xu, Y.-W. Yeh, G. Poirier, M. C. Mcalpine, R. A. Register, and N. Yao, "Flexible Piezoelectric PMN−PT Nanowire-Based Nanocomposite and Device."

[15] K. Il Park *et al.*, "Highly-efficient, flexible piezoelectric PZT thin film nanogenerator on plastic substrates," *Adv. Mater.*, vol. 26, no. 16, pp. 2514–2520, 2014.

[16] C. J. Hu, Y. H. Lin, C. W. Tang, M. Y. Tsai, W. K. Hsu, and H. F. Kuo, "ZnO-coated carbon nanotubes: Flexible piezoelectric generators," *Adv. Mater.*, vol. 23, no. 26, pp. 2941–2945, 2011.

[17] K. Il Park *et al.*, "Piezoelectric BaTiO3 thin film nanogenerator on plastic substrates," *Nano Lett.*, vol. 10, no. 12, pp. 4939–4943, 2010.

[18] J.-M. Benoit, B. Corraze, S. Lefrant, W. J. Blau, P. Bernier, and O. Chauvet, "Transport

properties of PMMA-Carbon Nanotubes composites," *Synth. Met.*, vol. 121, pp. 1215–1216, 2001.

[19] R. B. Mathur, S. Pande, B. P. Singh, and T. L. Dhami, "Electrical and Mechanical Properties of Multi-Walled Carbon Nanotubes Reinforced PMMA and PS Composites," *Polym. Polym. Compos.*, vol. 16, no. 2, pp. 101–113, 2008.

[20] V. Choudhary, B. P. Singh, and R. B. Mathur, "Carbon Nanotubes and Their Composites," *Synth. Appl. Carbon Nanotub. Their Compos.*, pp. 193–222, 2013.

[21] R. P. Ummer, R. B, C. Thevenot, D. Rouxel, S. Thomas, and N. Kalarikkal, "Electric, magnetic, piezoelectric and magnetoelectric studies of phase pure ($BiFeO_3$–$NaNbO_3$)–(P(VDF-TrFE)) nanocomposite films prepared by spin coating," *RSC Adv.*, vol. 6, no. 33, pp. 28069–28080, 2016.

[22] P. Saini, V. Choudhary, B. P. Singh, R. B. Mathur, and S. K. Dhawan, "Polyaniline-MWCNT nanocomposites for microwave absorption and EMI shielding," *Mater. Chem. Phys.*, vol. 113, no. 2–3, pp. 919–926, 2009.

[23] Q. Xiao and X. Zhou, "The study of multiwalled carbon nanotube deposited with conducting polymer for supercapacitor," *Electrochim. Acta*, vol. 48, no. 5, pp. 575–580, 2003.

[24] H. Xia, Q. Wang, K. Li, and G. H. Hu, "Preparation of polypropylene/carbon nanotube composite powder with a solid-state mechanochemical pulverization process," *J. Appl. Polym. Sci.*, vol. 93, no. 1, pp. 378–386, 2004.

[25] T. M. Wu and E. C. Chen, "Preparation and characterization of conductive carbon

nanotube-polystyrene nanocomposites using latex technology," *Compos. Sci. Technol.*, vol. 68, no. 10–11, pp. 2254–2259, 2008.

[26] O. Regev, P. N. B. ElKati, J. Loos, and C. E. Koning, "Preparation of Conductive Nanotube–Polymer Composites Using Latex Technology," *Adv. Mater.*, vol. 16, no. 3, pp. 248–251, 2004.

[27] B. Vigolo *et al.*, "Macroscopic Fibers and Ribbons of Oriented Carbon Nanotubes," *Am. Assoc. Adv. Sci.*, vol. 290, no. 5495, pp. 1331–1334, 2000.

[28] C. Dhand, S. K. Arya, S. P. Singh, B. P. Singh, M. Datta, and B. D. Malhotra, "Preparation of polyaniline/multiwalled carbon nanotube composite by novel electrophoretic route," *Carbon N. Y.*, vol. 46, no. 13, pp. 1727–1735, 2008.

[29] J. N. Coleman, U. Khan, W. J. Blau, and Y. K. Gun'ko, "Small but strong: A review of the mechanical properties of carbon nanotube-polymer composites," *Carbon N. Y.*, vol. 44, no. 9, pp. 1624–1652, 2006.

[30] N. Ramaratnam, Arun, and Jalili, "Reinforcement of Piezoelectric Polymers with Carbon Nanotubes: Pathway to Next-generation Sensors," *J. Intell. Mater. Syst. Struct.*, vol. 17, no. 3, pp. 199–208, 2006.

[31] D. Lee, H. P. Hong, C. J. Lee, C. W. Park, and N. K. Min, "Microfabrication and characterization of spray-coated single-wall carbon nanotube film strain gauges," *Nanotechnology*, vol. 22, p. 455301, 2011.

[32] K. J. Loh, J. Kim, J. P. Lynch, N. W. S. Kam, and N. a Kotov, "Multifunctional layer-by-layer carbon nanotube–polyelectrolyte thin films for strain and corrosion sensing," *Smart*

Mater. Struct., vol. 16, no. 2, pp. 429–438, 2007.

[33] S. V Anand and D. Roy Mahapatra, "Quasi-static and dynamic strain sensing using carbon nanotube/epoxy nanocomposite thin films," *Smart Mater. Struct.*, vol. 18, no. 4, p. 45013, 2009.

[34] M. H. Zhao, Z. L. Wang, and S. X. Mao, "Piezoelectric characterization individual zinc oxide nanobelt probed by piezoresponse force microscope," *Nano Lett.*, vol. 4, no. 4, pp. 587–590, 2004.

[35] M. Laurenti *et al.*, "Evaluation of the piezoelectric properties and voltage generation of flexible zinc oxide thin films," *Nanotechnology*, vol. 26, no. 21, p. 215704, 2015.

[36] S. Kessler and S. Spearing, "Design of a piezoelectric-based structural health monitoring system for damage detection in composite materials," *Proc. SPIE*, vol. 4701, pp. 86–96, 2002.

[37] M. Ruotsalainen, J. Jylha, and A. Visa, "Minimizing Fatigue Damage in Aircraft Structures," *IEEE Intell. Syst.*, vol. 31, no. 4, pp. 22–29, 2016.

[38] V. D. Vijayanand, V. Ganesan, and K. Laha, "New insights to damage initiation during creep deformation of stainless steel weld joints," *Mater. Sci. Eng. A*, vol. 703, no. July, pp. 37–44, 2017.

[39] V. Giurgiutiu and A. Zagrai, "Damage Detection in Thin Plates and Aerospace Structures with the Electro-Mechanical Impedance Method," *Struct. Heal. Monit.*, vol. 4, no. 2, pp. 99–118, 2005.

[40] R. Zhou, Yun-Lai, Figueiredo, E., Maia, N., Sampaio, R., Perera, "Damage detection in

structures using a transmissibility-based Mahalanobis distance," *Struct. Control Heal. Monit.*, vol. 22, pp. 1209–1222, 2015.

[41] W. Zhang, H. Hao, J. Wu, J. Li, H. Ma, and C. Li, "Detection of minor damage in structures with guided wave signals and nonlinear oscillator," *Measurement*, 2017.

[42] S. Park, S. Ahmad, C.-B. Yun, and Y. Roh, "Multiple Crack Detection of Concrete Structures Using Impedance-based Structural Health Monitoring Techniques," *Exp. Mech.*, vol. 46, no. 5, pp. 609–618, 2006.

[43] B. Huang and H. S. Kim, "Frequency response analysis of a delaminated smart composite plate," *J. Intell. Mater. Syst. Struct.*, vol. 26, no. 9, pp. 1091–1102, 2015.

[44] W. Lestari and S. Hanagud, "Health monitoring of structures - Multiple delamination dynamics in composite beams," *Am. Inst. Aeronaut. Astronaut.*, pp. 1–10, 1999.

[45] S. Kamila, "Introduction, classification and applications of smart materials: An overview," *Am. J. Appl. Sci.*, vol. 10, no. 8, pp. 876–880, 2013.

[46] G. Akhras, "Smart Materials and Smart Systems for the Future," *Can. Mil. J.*, pp. 25–32, 2000.

[47] Y. J. Yan and L. H. Yam, "Online detection of crack damage in composite plates using embedded piezoelectric actuators/sensors and wavelet analysis," *Compos. Struct.*, vol. 58, no. 1, pp. 29–38, 2002.

[48] G. Dib, E. Koricho, O. Karpenko, M. Haq, and L. Udpa, "Feasibility of PZT Ceramics for Impact Damage Detection in Composite Structures," *AIP Conf. Proc.*, vol. 1650, pp. 1072–1080, 2015.

[49] M. Dziendzikowski, A. Kurnyta, K. Dragan, S. Klysz, and A. Leski, “In situ Barely Visible Impact Damage detection and localization for composite structures using surface mounted and embedded PZT transducers: A comparative study,” *Mech. Syst. Signal Process.*, vol. 78, no. 2016, pp. 91–106, 2015.

[50] Z. L. Wang and W. Zhong Lin, “Zinc oxide nanostructures: growth, properties and applications,” *J. Phys. Condens. Matter*, vol. 16, no. 25, pp. R829–R858, 2004.

[51] S. Hingorani, V. Pillai, P. Kumar, M. S. Multani, and D. O. Shah, “Microemulsion Mediated Synthesis of Zinc-Oxide Nanoparticels for Varistor Studies,” *Mater. Res. Bull.*, vol. 28, no. 12, pp. 1303–1310, 1993.

[52] H. Rodríguez-Tobías, G. Morales, O. Rodríguez-Fernández, and P. Acuña, “Mechanical and UV-shielding properties of in situ synthesized poly(acrylonitrile-butadiene-styrene)/zinc oxide nanocomposites,” *J. Appl. Polym. Sci.*, vol. 127, no. 6, pp. 4708–4718, 2013.

[53] “Polyvinyl alcohol-carbon coated zinc oxide nanocomposites Electrical.” .

[54] P. Jood *et al.*, “Al-doped zinc oxide nanocomposites with enhanced thermoelectric properties,” *Nano Lett*, vol. 11, no. 10, pp. 4337–4342, 2011.

[55] H.-M. Lin, S.-J. Tzeng, P.-J. Hsiau, and W.-L. Tsai, “Electrode effects on gas sensing properties of nanocrystalline zinc oxide,” *Nanostructured Mater.*, vol. 10, no. 3, pp. 465–477, 1998.

[56] J. A. Rodriguez, T. Jirsak, J. Dvorak, S. Sambasivan, and D. Fischer, “Reaction of NO with Zn and ZnO : Photoemission , XANES , and Density Functional Studies on the

Formation of NO3," no. 2, pp. 319–328, 2000.

[57] P. X. Gao, Y. Ding, W. Mai, W. L. Hughes, C. Lao, and Z. L. Wang, "Conversion of zinc oxide nanobelts into superlattice-structured nanohelices," *Science (80-.).*, vol. 309, no. 5741, pp. 1700–4, 2005.

[58] L. Gao, Q. Li, W. Luan, H. Kawaoka, T. Sekino, and K. Niihara, "Preparation and Electric Properties of Dense Nanocrystalline Zinc Oxide Ceramics," *Am. Ceram. Soc.*, vol. 85, no. 4, pp. 1016–1018, 2002.

[59] N. F. C. Ooray, K. K. Ushiya, A. F. Ujimaki, and D. O. Kumura, "Optimization of Al-doped ZnO Window Layers for Large-Area Cu (InGa) Se 2 -Based Modules by RF / DC / DC Multiple Magnetron Sputtering," *Jpn. J. Appl. Phys.*, vol. 38, no. 11, pp. 6213–6218, 1999.

[60] A. Becheri, M. Durr, P. Lo Nostro, and P. Baglioni, "Synthesis and characterization of zinc oxide nanoparticles: Application to textiles as UV-absorbers," *J. Nanoparticle Res.*, vol. 10, no. 4, pp. 679–689, 2008.

[61] H. K. Yadav and V. Gupta, "A comparative study of ultraviolet photoconductivity relaxation in zinc oxide (ZnO) thin films deposited by different techniques," *J. Appl. Phys.*, vol. 111, no. 10, 2012.

[62] M. D. Spring, "Design of Zinc Oxide Tetrapod Devices," 2007.

[63] B. Kumar, K. Smita, L. Cumbal, and A. Debut, "Green approach for fabrication and applications of zinc oxide nanoparticles," *Bioinorg. Chem. Appl.*, vol. 2014, 2014.

[64] F. Verbakel, S. C. J. Meskers, and R. A. J. Janssen, "Electronic memory effects in diodes

of zinc oxide nanoparticles in a matrix of polystyrene or poly(3-hexylthiophene)," *J. Appl. Phys.*, vol. 102, no. 8, 2007.

[65] a Yadav *et al.*, "Functional finishing in cotton fabrics using zinc oxide nanoparticles," *Bull. Mater. Sci.*, vol. 29, no. 6, pp. 641–645, 2006.

[66] S. Talam, S. R. Karumuri, and N. Gunnam, "Synthesis, Characterization, and Spectroscopic Properties of ZnO Nanoparticles," *ISRN Nanotechnol.*, vol. 2012, pp. 1–6, 2012.

[67] A. Moezzi, A. M. McDonagh, and M. B. Cortie, "Zinc oxide particles: Synthesis, properties and applications," *Chem. Eng. J.*, vol. 185–186, pp. 1–22, 2012.

[68] E. Hernández, C. Goze, P. Bernier, and R. A, "Elastic properties of single-wall nanotubes," *Appl. Phys. A*, vol. 292, pp. 287–292, 1999.

[69] L. Vaccarini, C. Goze, L. Henrard, E. Hernández, P. Bernier, and A. Rubio, "Mechanical and electronic properties of carbon and boron-nitride nanotubes," *Carbon N. Y.*, vol. 38, no. 11, pp. 1681–1690, 2000.

[70] O. Lourie and H. D. Wagner, "Evaluation of Young's modulus of carbon nanotubes by micro-Raman spectroscopy," *J. Mater. Res.*, vol. 13, no. 9, pp. 2418–24, 1998.

[71] M.-F. Yu, B. S. Files, S. Arepalli, and R. S. Ruoff, "Tensile Loading of Ropes of Single Wall Carbon Nanotubes and their Mechanical Properties," *Phys. Rev. Lett.*, vol. 84, no. 24, pp. 5552–5555, 2000.

[72] A. M. Yu *et al.*, "Strength and Breaking Mechanism of Multiwalled Carbon Nanotubes Under Tensile Load," vol. 287, no. 5453, pp. 637–640, 2000.

[73] T. T. Ebbesen, T. W., Lezec H. J., Hiura H., Bennett J. W., Ghaemi H. F, “Electrical conductivity of individual carbon nanotubes,” *Nature*, vol. 382. pp. 54–56, 1996.

[74] S. Iijima, “Helical microtubules of graphitic carbon,” *Nature*, vol. 354, pp. 56–58, 1991.

[75] M. F. L. De Volder, S. H. Tawfick, R. H. Baughman, and A. J. Hart, “Carbon Nanotubes: Present and Future Commercial Applications,” *Sci. Mag. (New York, NY)*, vol. 339, no. 6119, pp. 535–539, 2013.

[76] I. Kang, M. J. Schulz, J. H. Kim, V. Shanov, and D. Shi, “A carbon nanotube strain sensor for structural health monitoring,” *Smart Mater. Struct*, vol. 15, pp. 737–748, 2006.

[77] G. T. Pham, Y. Bin Park, Z. Liang, C. Zhang, and B. Wang, “Processing and modeling of conductive thermoplastic/carbon nanotube films for strain sensing,” *Compos. Part B Eng.*, vol. 39, no. 1, pp. 209–216, 2008.

[78] N. Saber *et al.*, “Superior piezoelectric composite films: taking advantage of carbon nanomaterials.,” *Nanotechnology*, vol. 25, no. 4, p. 45501, 2014.

[79] M. S. P. Shaffer and A. H. Windle, “Fabrication and characterization of carbon nanotube/poly(vinyl alcohol) composites,” *Adv. Mater.*, vol. 11, no. 11, pp. 937–941, 1999.

[80] R. Andrews, D. Jacques, D. Qian, and T. Rantell, “Multiwall carbon nanotubes: Synthesis and application,” *Acc. Chem. Res.*, vol. 35, no. 12, pp. 1008–1017, 2002.

[81] B. P. Singh *et al.*, “Designing of multiwalled carbon nanotubes reinforced low density polyethylene nanocomposites for suppression of electromagnetic radiation,” *J. Nanoparticle Res.*, vol. 13, no. 12, pp. 7065–7074, 2011.

[82] K. L. Lu, R. M. Lago, Y. K. Chen, M. L. H. Green, P. J. F. Harris, and S. C. Tsang, “Mechanical damage of carbon nanotubes by ultrasound,” *Carbon N. Y.*, vol. 34, no. 6, pp. 814–816, 1996.

[83] W. C. Oliver and G. M. Pharr, “An improved technique for determining hardness and elastic modulus using load and displacement sensing indentation experiments,” *J. Mater. Res. Soc.*, vol. 7, no. 6, pp. 1564–1583, 1992.

[84] K. Evanoff *et al.*, “Towards ultrathick battery electrodes: Aligned carbon nanotube-enabled architecture,” *Adv. Mater.*, vol. 24, no. 4, pp. 533–537, 2012.

[85] C. Sotowa *et al.*, “The Reinforcing Effect of Combined Carbon Nanotubes and Acetylene Blacks on the Positive Electrode of Lithium-Ion Batteries,” *ChemSucChem*, vol. 1, pp. 911–915, 2008.

[86] L. Dai, D. W. Chang, J.-B. Baek, and W. Lu, “Carbon nanomaterials for advanced energy conversion and storage.,” *Small*, vol. 8, no. 8, pp. 1130–66, 2012.

[87] S. C. Sun, C. Y. Huang, C. M. Hsu, and J. H. Kuang, “The Effect of Nano-Scale Local Defects on Mechanical Properties of Silicon and Diamond Films,” *Integr. Ferroelectr.*, vol. 143, no. 1, pp. 1–9, 2013.

[88] M. B. Bryning, D. E. Milkie, M. F. Islam, J. M. Kikkawa, and A. G. Yodh, “Thermal conductivity and interfacial resistance in single-wall carbon nanotube epoxy composites,” *Appl. Phys. Lett.*, vol. 87, no. 16, pp. 1–3, 2005.

[89] E. P. Koumoulos, P. Jagadale, A. Lorenzi, A. Tagliaferro, and C. A. Charitidis, “Evaluation of surface properties of epoxy-nanodiamonds composites,” *Compos. Part B*

Eng., vol. 80, pp. 27–36, 2015.

Appendix A: MATLAB code for numerical solutions

The MATLAB Code used for the theoretical modeling and simulation of the delaminated cantilever beam with its top surface covered by a piezoelectric coating in Chapter 3 is shown below as a reference.

```
clc; clear;

% Properties of the material

L=1.0; L1=0.3; a=0.4; L2=L1+a;

p=8000; b=0.05;

Pi=3.1415926;

E=2*10^11;

I1=b*(0.01)^3/12; I2=b*(0.005)^3/12; I3=b*(0.005)^3/12;

a1=(p*b*0.01); a2=(p*b*0.005); a3=(p*b*0.005);

T=E*I1; T12=E*I2;  T23=E*I3;

charge=[];
Voutput=[];

%% check the eigen value of the parametric matrix (find the system
resonant
%% frequency with certain voltage gains)

% for gg=1.3:1.2:2.5
% %g=0.001;
% g=gg*Cv;
i=1;j=1;


for w=0:0.01:1000;

  x(i)=w;

  k1=(a1*w^2/T)^0.25; k2=(a2*w^2/(T12))^0.25; k3=(a3*w^2/(T23))^0.25;


    M=[1,0,1,0,0,0,0,0,0,0,0,0,0,0,0,0;...
    0,k1,0,k1,0,0,0,0,0,0,0,0,0,0,0,0;...
```

```
    cos(k1*L1),sin(k1*L1),cosh(k1*L1),sinh(k1*L1),-1,0,-
1,0,0,0,0,0,0,0,0,0;...
    cos(k1*L1),sin(k1*L1),cosh(k1*L1),sinh(k1*L1),0,0,0,0,-1,0,-
1,0,0,0,0,0;...

    -sin(k1*L1)*k1,cos(k1*L1)*k1,sinh(k1*L1)*k1,cosh(k1*L1)*k1,0,-
k2,0,-k2,0,0,0,0,0,0,0,0;...
    -
sin(k1*L1)*k1,cos(k1*L1)*k1,sinh(k1*L1)*k1,cosh(k1*L1)*k1,0,0,0,0,0,-
k3,0,-k3,0,0,0,0;...

    -T*cos(k1*L1)*k1^2,-
T*sin(k1*L1)*k1^2,T*cosh(k1*L1)*k1^2,T*sinh(k1*L1)*k1^2,...
    T12*k2^2,0,-T12*k2^2,0,T23*k3^2,0,T23*k3^2,0,0,0,0,0;...
    -T*sin(k1*L1)*k1^3,T*cos(k1*L1)*k1^3,-T*sinh(k1*L1)*k1^3,-
T*cosh(k1*L1)*k1^3,0,-T12*k2^3,0,T12*k2^3,0,-
T23*k3^3,0,T23*k3^3,0,0,0,0;...


    0,0,0,0,cos(k2*a),sin(k2*a),cosh(k2*a),sinh(k2*a),0,0,0,0,-1,0,-
1,0;...
    0,0,0,0,0,0,0,0,cos(k3*a),sin(k3*a),cosh(k3*a),sinh(k3*a),-1,0,-
1,0;...

    0,0,0,0,-
sin(k2*a)*k2,cos(k2*a)*k2,sinh(k2*a)*k2,cosh(k2*a)*k2,0,0,0,0,0,-
k1,0,-k1;...
    0,0,0,0,0,0,0,0,-
sin(k3*a)*k3,cos(k3*a)*k3,sinh(k3*a)*k3,cosh(k3*a)*k3,0,-k1,0,-k1;...

    0,0,0,0,-T12*cos(k2*a)*k2^2,-
T12*sin(k2*a)*k2^2,T12*cosh(k2*a)*k2^2,T12*sinh(k2*a)*k2^2,...
    -T23*cos(k3*a)*k3^2,-
T23*sin(k3*a)*k3^2,T23*cosh(k3*a)*k3^2,T23*sinh(k3*a)*k3^2,T*k1^2,0,-
T*k1^2,0;...

    0,0,0,0,T12*sin(k2*a)*k2^3,-
T12*cos(k2*a)*k2^3,T12*sinh(k2*a)*k2^3,T12*cosh(k2*a)*k2^3,T23*sin(k3*
a)*k3^3,-T23*cos(k3*a)*k3^3,...
    T23*sinh(k3*a)*k3^3,T23*cosh(k3*a)*k3^3,0,T*k1^3,0,-T*k1^3;...

    0,0,0,0,0,0,0,0,0,0,0,0,cos(k1*(L-L2))*k1^2,sin(k1*(L-L2))*k1^2,-
cosh(k1*(L-L2))*k1^2,-sinh(k1*(L-L2))*k1^2;...
    0,0,0,0,0,0,0,0,0,0,0,0,-sin(k1*(L-L2))*k1^3,cos(k1*(L-L2))*k1^3,-
sinh(k1*(L-L2))*k1^3,-cosh(k1*(L-L2))*k1^3];
    %M/100;

     dm(i)=det(M);

    if ((i>=2) && ((dm(i-1)*dm(i))<0))
        W(j)=(x(i-1)+x(i))/2; % value of natrural angular frequency
        f(j)=W(j)/(2*Pi); %nature frequency
```

```
        j=j+1;
    end
        i=i+1;
end

%%

W  %value of nature rotating speed
f  %value of frequency



% plot(x,dm);
% G(tt)=gg;
% fre1(tt)=f(1);
% ww=f(1)*2*Pi;
% tt=tt+1;
% end

for n=1:3

    w=W(n);
    k1=(a1*w^2/T)^0.25; k2=(a2*w^2/(T12))^0.25;
k3=(a3*w^2/(T23))^0.25;


    M=[1,0,1,0,0,0,0,0,0,0,0,0,0,0,0,0;...
    0,k1,0,k1,0,0,0,0,0,0,0,0,0,0,0,0;...

    cos(k1*L1),sin(k1*L1),cosh(k1*L1),sinh(k1*L1),-1,0,-
1,0,0,0,0,0,0,0,0,0;...
    cos(k1*L1),sin(k1*L1),cosh(k1*L1),sinh(k1*L1),0,0,0,0,-1,0,-
1,0,0,0,0,0;...

    -sin(k1*L1)*k1,cos(k1*L1)*k1,sinh(k1*L1)*k1,cosh(k1*L1)*k1,0,-
k2,0,-k2,0,0,0,0,0,0,0,0;...
    -
sin(k1*L1)*k1,cos(k1*L1)*k1,sinh(k1*L1)*k1,cosh(k1*L1)*k1,0,0,0,0,0,-
k3,0,-k3,0,0,0,0;...

    -T*cos(k1*L1)*k1^2,-
T*sin(k1*L1)*k1^2,T*cosh(k1*L1)*k1^2,T*sinh(k1*L1)*k1^2,...
    T12*k2^2,0,-T12*k2^2,0,T23*k3^2,0,T23*k3^2,0,0,0,0,0;...
    -T*sin(k1*L1)*k1^3,T*cos(k1*L1)*k1^3,-T*sinh(k1*L1)*k1^3,-
T*cosh(k1*L1)*k1^3,0,-T12*k2^3,0,T12*k2^3,0,-
T23*k3^3,0,T23*k3^3,0,0,0,0;...


    0,0,0,0,cos(k2*a),sin(k2*a),cosh(k2*a),sinh(k2*a),0,0,0,0,-1,0,-
1,0;...
    0,0,0,0,0,0,0,0,cos(k3*a),sin(k3*a),cosh(k3*a),sinh(k3*a),-1,0,-
1,0;...
```

```
    0,0,0,0,-
sin(k2*a)*k2,cos(k2*a)*k2,sinh(k2*a)*k2,cosh(k2*a)*k2,0,0,0,0,0,-
k1,0,-k1;...
    0,0,0,0,0,0,0,0,-
sin(k3*a)*k3,cos(k3*a)*k3,sinh(k3*a)*k3,cosh(k3*a)*k3,0,-k1,0,-k1;...

    0,0,0,0,-T12*cos(k2*a)*k2^2,-
T12*sin(k2*a)*k2^2,T12*cosh(k2*a)*k2^2,T12*sinh(k2*a)*k2^2,...
    -T23*cos(k3*a)*k3^2,-
T23*sin(k3*a)*k3^2,T23*cosh(k3*a)*k3^2,T23*sinh(k3*a)*k3^2,T*k1^2,0,-
T*k1^2,0;...

    0,0,0,0,T12*sin(k2*a)*k2^3,-
T12*cos(k2*a)*k2^3,T12*sinh(k2*a)*k2^3,T12*cosh(k2*a)*k2^3,T23*sin(k3*
a)*k3^3,-T23*cos(k3*a)*k3^3,...
    T23*sinh(k3*a)*k3^3,T23*cosh(k3*a)*k3^3,0,T*k1^3,0,-T*k1^3;...

    0,0,0,0,0,0,0,0,0,0,0,0,cos(k1*(L-L2))*k1^2,sin(k1*(L-L2))*k1^2,-
cosh(k1*(L-L2))*k1^2,-sinh(k1*(L-L2))*k1^2;...
    0,0,0,0,0,0,0,0,0,0,0,0,-sin(k1*(L-L2))*k1^3,cos(k1*(L-L2))*k1^3,-
sinh(k1*(L-L2))*k1^3,-cosh(k1*(L-L2))*k1^3];


M1=M(2:16,2:16);

M2=-M(2:16,1);

A(1,n)=1;
A(2:16,n)=inv(M1)*M2;


end

for n=1:3
w=W(n);
    k1=(a1*w^2/T)^0.25; k2=(a2*w^2/(T12))^0.25;
k3=(a3*w^2/(T23))^0.25;
i=1;

for x=0:0.001:L1
    Lx(i)=x;

WA(i,n)=A(1,n)*cos(k1*x)+A(2,n)*sin(k1*x)+A(3,n)*cosh(k1*x)+A(4,n)*sin
h(k1*x);
        i=i+1;
end
i=i-1;
for x=L1:0.001:L1+a
    Lx(i)=x;
    xx=x-L1;
```

```
WA(i,n)=A(5,n)*cos(k2*xx)+A(6,n)*sin(k2*xx)+A(7,n)*cosh(k2*xx)+A(8,n)*
sinh(k2*xx); % top surface

%WA(i,n)=A(9,n)*cos(k3*xx)+A(10,n)*sin(k3*xx)+A(11,n)*cosh(k3*xx)+A(12
,n)*sinh(k3*xx);%bottomsurface

        i=i+1;
end

j=1;
for x=L1:0.001:L1+a
    Lxb(j)=x;
    xx=x-L1;

WB(j,n)=A(9,n)*cos(k3*xx)+A(10,n)*sin(k3*xx)+A(11,n)*cosh(k3*xx)+A(12,
n)*sinh(k3*xx);
        j=j+1;
end

% for x=L1:0.001:L1+a
%     Lx(i)=x;
%     xx=x-L1;
%
WA(i,n)=A(9,n)*cos(k3*xx)+A(10,n)*sin(k3*xx)+A(11,n)*cosh(k3*xx)+A(12,
n)*sinh(k3*xx);
%         i=i+1;
% end
i=i-1;
for x=L2:0.001:L
    Lx(i)=x;
    xx=x-L2;

WA(i,n)=A(13,n)*cos(k1*xx)+A(14,n)*sin(k1*xx)+A(15,n)*cosh(k1*xx)+A(16
,n)*sinh(k1*xx);
        i=i+1;
end


end


figure(1);
plot(Lx,WA(:,1),'--'); hold on; plot(Lxb,WB(:,1),'-');
xlabel('Length of the beam (m), L');
ylabel(' Deflection, w(x)');
title('The vibration mode 1');

figure(2);
plot(Lx,WA(:,2),'--'); hold on; plot(Lxb,WB(:,2),'-');
xlabel('Length of the beam (m), L');
ylabel('Deflection, w(x)');
```

```
title('The vibration mode 2');

figure(3);
plot(Lx,WA(:,3),'--'); hold on; plot(Lxb,WB(:,3),'-');
xlabel('Length of the beam (m)');
ylabel('Deflection, w(x)');
title('The vibration mode 3');


%Determination of the steady state response

Tinitial = 0; Tfinal = 0.01;
dTime = 0.001;

%L=1.0; L1=0.3; a=0.2; L2=L1+a;

%p=8000; b=0.05;

%Pi=3.1415926;

%E=2*10^11;

%I1=b*(0.01)^3/12; I2=b*(0.005)^3/12; I3=b*(0.005)^3/12;

%a1=(p*b*0.01); a2=(p*b*0.005); a3=(p*b*0.005);

%a1 = b*0.005; %sectional area
% T=E*I1; T12=E*I2;  T23=E*I3;


fo = 10;
omega = 30;
e31=-2.8; Cv=0.75*10^-9; hPZT=0.0003; h=0.01;

% finding of the total beam response
t = 1; % counter through time to get 'qntMatrix'
    for Time = Tinitial: dTime : Tfinal % iterate through time
interval
%         Timepoint(tn)=Time;
        for n = 1:3; % iterate through mode shapes
            w=W(n);
            % integration for bdash----------------------------------------
---------
            dx = 0.001; % x increment for integration
            Xl = L2; % lower bound of integral dx
            Xu = L; % upper bound of integral dx
            numRectX = L/dx; % number of integration rectangles in
bdash integral

            bdash = 0; % setting back to zero after one loop over n
           % WA = @(x) A(13,n)*cos(k1*(x-L2))+A(14,n)*sin(k1*(x-
L2))+A(15,n)*cosh(k1*(x-L2))+A(16,n)*sinh(k1*(x-L2));
```

```
%       Wnx = @(x) ((An(1,n))* (cos(betaN(n)*x))) +  ((An(2,n))*
(sin(betaN(n)*x))) + ((An(3,n))* (cosh(betaN(n)*x))) + ((An(4,n))*
(sinh(betaN(n)*x))); % 'n'th mode shape

      dxl = Xl; % dx lower bound
      for i = 1:1:numRectX % for every rectangular element
        %dxu = dxl + dx; % dx upper bound
%         deltaAreaX(i) = dx * (WA((dxl + dxu)/2 )^2);
        deltaAreaX(i) = dx*WA(i,n)*WA(i,n);
        bdash = sum(deltaAreaX);
        %dxl = dxu;
      end


      % integration of QnT* sin(omegaN(t-T)---------------------
---------
      %WA = @(x) A(13,n)*cos(k1*(x-L2))+A(14,n)*sin(k1*(x-
L2))+A(15,n)*cosh(k1*(x-L2))+A(16,n)*sinh(k1*(x-L2));
%       WAL = WA(L)

      WAL = WA(length(WA(:,1)),n); % Wnx value at the edge of
the beam
      QnT(n) = fo * sin(omega*Time) * WAL;

%       syms T t;



      %qntMatrix(t,n) =@(t)(1/((a1*bdash) * W(n))) *
int(QnT*sin(W(n)*(t-T)),T,0,1);

      qntMatrix(t,n) = (1/((a1*bdash) * (W(n)^2 - omega^2))) *
QnT(n); %%%%%% qn(t) Use Duhamel integral?????

      % columns corresponding to modes and rows corresponding to
      % modal response at each time

      %WnLVector(n) = WAL; % Wnx values at x = L2
      %WLtMatrix(t,:) = WA(:,:)* qntMatrix(t,:);

    end

    WLtMatrix1(:,t) = WA(:,1)* qntMatrix(t,1);
    WLtMatrix2(:,t) = WA(:,2)* qntMatrix(t,2);
    WLtMatrix3(:,t) = WA(:,3)* qntMatrix(t,3);

WLtMatrix(:,t)=WLtMatrix1(:,t)+WLtMatrix2(:,t)+WLtMatrix3(:,t);
%
WLtMatrix(:,t)=WLtMatrix1(:,t)+WLtMatrix2(:,t)+WLtMatrix3(:,t);
%
% mode superposition-------------------------------------------------
%     element wise operation
```

```
                figure (4)
        plot(Lx', WLtMatrix(:,t)); hold on;
%
     xlabel('Length of the beam (m)');
     ylabel('deflection of the beam [w(x)]');
    title('The deflection of the beam after a dynamic excitation');


%         plot(Lx',Voltage(t)); hold on;

% Slopdiff(tn)=(WLtMatrix(Point2-2)- WLtMatrix(Point2-1))/0.001-
(WLtMatrix(Point1+2)- WLtMatrix(Point1+1))/0.001;
%
% Q=-e31*b*((h+hPZT)/2)*(Slopdiff(tn));
%
%
%     charge=[charge,Q];
%     Voltage = Q/Cv;
%
%     Voutput=[Voutput,Voltage];
%
%         figure (5)


        t = t + 1; % counter up


    end


for i=3:length(WLtMatrix(:,t-1))

diff1= (WLtMatrix(i,t-1)- WLtMatrix(i-1,t-1))/0.001;
diff2 = (WLtMatrix(i-1,t-1)- WLtMatrix(i-2,t-1))/0.001;
Slop(i-2)=(WLtMatrix(i,t-1)- WLtMatrix(i-1,t-1))/0.001;
Curvature(i-2)=(diff1-diff2)/0.001;

% Curvature(i-2)=((WLtMatrix(i)- WLtMatrix(i-1))/0.001- (WLtMatrix(i-
1)- WLtMatrix(i-2))/0.001)/0.001;

Q(i-2)=-e31*((h+hPZT)/2)*Curvature(i-2)*b*0.001;

i=i+1;

end
%     figure (1)
%     plot(Lx,WA);

%     figure (2);
%     Voltage = Q/Cv;
%     plot(Lx(1:(length(Lx)-2)),Voltage); % for the curvature
distribution at the last time point during the vibration.
```

```
%
%     xlabel('Length of the beam (m)');
%     ylabel('Voltage (V)');
%     title('Voltage generated by the piezoelectric patch');


     figure (5);
    Voltage = Q/Cv;
    plot(Lx(1:(length(Lx)-2)),Voltage); % for the curvature
distribution at the last time point during the vibration.

    xlabel('Length of the beam (m)');
    ylabel('Voltage (V)');
    title('Voltage generated by the piezoelectric coating');


%WLt = sum(WLtMatrix,2); % w(L1,t) vector having responses of the
beam, summing of column values



% figure(5)
% time = Tinitial: dTime : Tfinal;
% plotCurve = plot(time, WLtMatrix(length(WLtMatrix),:));
```